Received: 14 September 2022 | Revised: 07 October 2022 | Accepted: 17 October 2022

https://doi.org/10.56946/jce.v1i01.49

Journal of Chemistry and Environment

REVIEW

Comprehensive Review on Synthesis of Abox Material and its Catalytic Applications

Syeda Mehak Batool[1], Khushbo e Kainat[1], Suqqyana Fazal[1], Fawad Ahmad[1*]

[1]Department of Chemistry, University of Wah, Quaid Avenue, Wah Cantt., (47010), Punjab, Pakistan
Corresponding author:
fawad.ahmad@uow.edu.pk

Abstract

Perovskites are materials with crystal structures comparable to perovskite (mineral). The backbone of perovskite is calcium titanium oxide ($CaTiO_3$). Perovskite oxides with the general formula ABO_x are highly important. In the general formula of perovskite ABX_3, A & B are cations, where X is an anion that binds with two cations. Perovskites have proven their versatility in catalysis, photovoltaics, solar cells, electrode conducting material, etc. Due to their unique structural properties and applications, they are compatible with elements having metallic approximately 90% of the periodic table.This review discusses the synthesis and catalytic application of perovskite oxides. There are five sections to this review: (a) a brief description of perovskite oxides, (b) the synthesis of perovskite oxides with various properties, (c) general characterization, (d) catalytic applications, and (e) conclusions and future perspectives.

Keywords: perovskite oxides, synthesis, catalysis.

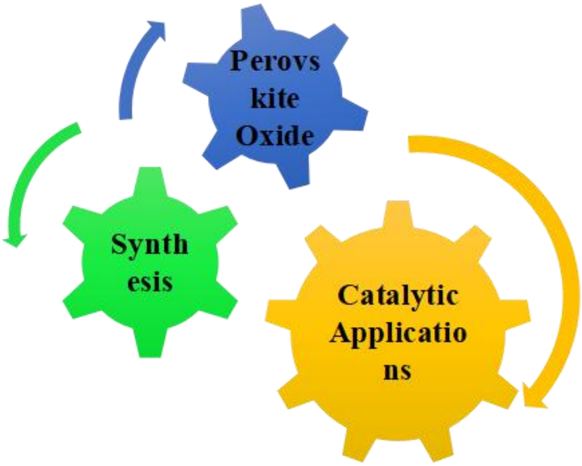

Graphical Abstract

1. Introduction

The term perovskite is used to explain oxides produced from Ca-Ti-O_3 with the structural formula ABO_3 or A_2BO_4. Oxides of A_2BO_4, are often known as perovskite-like oxides. They are synthesized by alternating ABO_3 and AO layers. The cations A and B were replaced by a new cation with a different oxidation state and radius, and the material noted for its structural stability. The oxidation state of the B-site cation and the number of oxygen vacancies may be regulated when a desired external cation is used, providing a practical and workable technique for connecting physicochemical characteristics with the catalytic ability of the material [1].

According to several experts, perovskite oxides have been used to generate a range of oxygenated molecules [2].Due to their significant thermal stability, the exceptional activity of oxidation and low cost, perovskites has examined for a range of automobile exhaust purification, fuel cells, N_2O decompositions and Water Gas Shift WGS reactions. Perovskite oxide having lanthanide at the A site and transitional metals at the B site is more frequently utilized within heterogeneous catalysis, possibly to use transition metals' catalytic capabilities. Noble metals are recommended as a catalyst owing to their excellent stability in these circumstances. Whereas transition metals have good catalytic activity because of their electronic structure, transitional metals could oxidize in higher temperatures within oxygen presence [3]. Larger ionic radius cations have oxygen atoms and there is 12-fold coordination accommodating sites A and a cation having lower ionic radius with 6-folded coordination accommodating sites B. Perovskite oxides have a structure of the cubical crystal. B is located in the cubic closet packing’s octahedral gaps formed by A and O [3].

As stated in “Witness to grace” Professor John began his research to explore perovskite materials 60 years ago and explored perovskite materials for their applications for storage and energy conversion [4]. Most catalysts used are made of mixed metal oxides. Out of mixed metal oxides, a perovskite-type oxide was highlighted. Despite ionic radius requirements, another requirement is electro-neutrality, which means the sum of charges on cations is equal to the charge on anion, which can be achieved only by proper distribution of charge on A, B, and O, respectively. According to Pena and Flerro et al., [5] perovskite oxide materials, such as ABO_3, have exceptional properties of physical like ($BaTiO_3$) Ferro electricity, ($SrRuO_3$) ferromagnetism, ($LaFeO_3$) weak ferromagnetism, ($YBa_2Cu_3O_7$) superconductivity and thermally conductive. They also examined the adsorption features of many perovskite materials by studying their shape to find their active sites, which they then investigated for catalytic activity. Perovskite oxides with different morphologies are shown in Fig (1).

Catalysis is a reaction in which the outcome is influenced by a chemical known as the catalyst, which is not consumed during the reaction. Catalysis can be either homogeneous or heterogeneous. The mixture reaction and the catalyst are in the uni-phase in homogeneous catalysis, whereas the mixture reaction and the catalyst are in separate phases in heterogeneous catalysis. Both types of catalysis have high activity, but heterogeneous catalysis has low selectivity than homogeneous catalysis.

Heterogeneous catalysis requires high reaction temperature than homogeneous catalysis. However, our main aim in this study is to focus on the preparation method of perovskite oxide and explore its catalytic application, which provides the basis for all.

1.1 Perovskite Materials' (Properties of Electronic, Magnetic, and Optical)

The study of oxides of perovskite magnetic properties has attracted a lot of curiosity, among other things. There have already been findings of magneto-optical materials, sensors, catalysts, fuel cells, and other applications. Transition metal perovskite oxides have recently gotten attention because of their significant magnetic properties. Because of the great interaction of electron-electron to the manifold 3D, and their physical strength, these perovskite oxides have remarkable magnetic properties.

Perovskites are used within solar cells, and light detectors and light-emitting diodes are examples of this, for example, optoelectronic applications (LEDs). Because of their outstanding optical features, which are required for both light absorbers and light-generating materials, they are prominent. Higher coefficients of absorption and configurable bandgaps of direct, for example. As a result, in the dye of solid-state comparison sensitized solar cells, the thickness of TiO_2 within perovskite solar cells is relatively lower. It could enhance to some extent, that perovskite solar cells are commercialized and developed.

2. Perovskite Oxides Synthesis with different morphologies

2.1 Perovskite Oxides synthesis in Bulk

Mixed oxides of perovskites are generated by simply annealing a metal oxide mixture at a high temperature, which is a straightforward process. This synthesis is environmentally beneficial because it occurs without the release of any hazardous gases as a result of the reaction. Although it is necessary to homogenize the metal oxide precursors for them to react completely and generate pure perovskite oxides, this is not required. In this case, the mixture could be processed in ethanol with a ball mill or stabilized ZrO_2 balls. When good mechanical attributes are required, this approach generates a sample with a lesser surface area and a greater particle size, which is often used in ceramics [1].

Because catalysis is a surface reaction, it necessitates strong contact between the catalyst and the substrate. And, to put catalysis into practice, perovskite oxides must have a larger surface area and a smaller particle size. As a result, high-surface-area perovskite oxides must be synthesized. Because the precursor and synthesis processes have complex organic that is employed to correlate, burn, and finally, metal oxide particles disperse, replacing metal oxides with soluble metal nitrates is one of the most successful approaches. Citric acid combustion, for example, uses metal nitrates as a precursor and citric- acid as a complex organic to metal coordinate ions. Because of its simple operating technique and high catalytic performance, this technique is frequently used to make oxides of perovskite catalysts within catalysis [1].

Undesirable gases like NO_2 and CO_2 are emitted in the process due to nitrates and organic compounds. As a result, synthesis should be done in a fume cupboard or somewhere with good ventilation. It should also be highlighted that because the organic complex contains a carbon source, the creation of carbonates is unavoidable. Carbonates may influence the material's catalytic effectiveness in some reactions; hence their amount should be kept as low as feasible [1].

2.2 Nano-Sized Perovskite Oxides

Following is the procedure for making perovskite oxides from polyvinyl pyrrolidone (PVP):

A solution of water containing metal stoichiometric nitrates and Poly-Vinyl-Pyrrolidone was heated to 100 degrees Celsius. Perovskite-type oxide precursor produced after 1 hour of drying at 150°C. The polymerized precursors were burned in the presence of air for 6 hours at 300–600 degrees Celsius, yielding perovskite-type oxides [6].

Also in the PVP technique, a reaction of solid-state and a procedure of citrate was used to make $La_{0.6}Sr_{0.4}Mn_{0.6}Fe_{0.4}O_3$. La_2O_3, MnO_2, $SrCO_3$, and Fe_2O_3 were used as starting particles for the solid-state reaction. The powders were mixed well in an agate mortar, and the mixture was sintered in the air for 10 hours at 400–1300°C. Nitrates of metal and citric-acid-monohydrate ($C_6\,H_8\,O_7.H_2O$; 2 times total cation moles; double the times of total moles of cations) dissolve in water and agitate at about 100°C till gel formation. A precursor was created after gel drying for 1 hour at about 150°C. The precursor was calcined within the atmosphere for 10 hours about 4–8 hundred degrees Celsius. Temperature raised with a continuous rate of about $20^{o}C\ min^{-1}$ for calcination [6].

According to SEM analysis, the oxide manufactured with PVP was 20nm to 30nm in size, whereas those made with the process of citrate and the reaction of solid state were 50 nm and 10 nm in size. $La_{0.6}Sr_{0.4}Mn_{0.6}Fe_{0.4}O_3$ obtained from PVP had the lowest sized particle and the biggest surface-area specific of the several synthetic techniques, probably due to calcination could be done for low temperatures of about 600 ^{0}C [6]. The typical preparation technique for perovskite-type oxides using polyol mediates synthesis is presented in scheme 1 [7].

2.3 Porous Perovskite Oxides

2.3.1. Synthesis in solid state

To manufacture perovskite oxides, a reaction of solid state is typically utilized, characterized by a simpler process, higher calcination temperature, mass-production capabilities, and lesser manufacturing cost, among other things [8]. In a typical synthesis, the solid raw components are thoroughly mixed before being calcined at a higher temperature for a long enough period to generate a suitable phase of perovskite oxide.

A calcination temperature of over 900 °C is required to produce phase-pure perovskite oxides due to the significance of overcoming the diffusion barrier for perovskite phase formation during the synthesis [8-10]. Particularly for perovskite oxides, including several components and alkaline earth elements, higher calcination temperatures and a lengthy calcination duration of several hours are necessary to produce a high-purity perovskite phase [11-13]. On the other hand, such high synthesis temperatures usually lead to poor sintering and nearly pore-free products. A lower phase formation temperature is required efficiently synthesize porous oxides of perovskite utilizing the reaction of solid-state methodology, and achieving good perovskite phase purity at a lower annealing temperature is a severe difficulty [14].

Solid-state synthesis with the help of high-energy ball milling (HEBM) [13,15-20] and Solid-state reaction injected into the molten salt [21-24] are two recently founded solid-state reaction processes that have been updated. In the solid-state synthesis of HEBM-assisted, known as mechano-chemical manufacture, mechanical energy is frequently used to aid the reaction of solid-state. In process of preparation, mechanical force is used to break down the reactants and products into small particles and appropriately mix them. As a result, the phase formation diffusion barrier can be reduced effectively, the preparation temperature may be properly reduced, and the product surface specific area can successfully be increased. Various perovskite oxides have been successfully generated using this process to utilize as electrodes in metal atmosphere batteries and Solid Oxide Fuel Cell SOFCs [25-28]. The ball-milling period, ball mass ratio to powder solid and other operational factors influence the product surface specific area, pores structure, and size of crystalline [26-29]. High Energy Ball Milling HEBM-assisted solid-state synthesis still has poor porosity which is a severe disadvantage [14]. When a sample is placed under stress calcination, the pores structure is prone to collapse. Kaliaguine's team changed the HEBM-assisted solid-state synthesis technique by adding various alkali additives to the 4–105 m^2 g^{-1} ball-milling process to make porous perovskites, which maximized porosity [30,31]. As a result, they all have outstanding catalytic characteristics in a variety of procedures. To our knowledge, no study on applying this fascinating technique to the fabrication of perovskite electro-catalysts in ORR or OER processes has been published, emphasizing that much more research is needed in this domain. If this novel method was used to create porous perovskites as ORR/OER electro-catalysts, the impurity from the alkali additive could potentially be introduced into the perovskite phase and the potential change in activity could be attributed to such impurity doping because most elements can be doped into the perovskite lattice [14]. Inadequate porosity is produced by the reformative HEBM-assisted synthesis method described above because insufficient amounts of alkali are supplied. The molten salt synthesis method, which uses a large amount of alkali metal salts to generate crystallized, chemically purified single-phase powder has gotten more attention in recent history due to its simple, versatile, cost-effective approach [21-24, 32-34]. The molten salt additions serve as a soft template as well as a heat source [33-35]. In synthesis low melting point salts are combined to reactants in non-solvent freshly ground form crystals and the combined precursors are then heated to temperature over the salts melting point. Because reactants have a defined solubility in liquid salts, the molten salt methodology is used [18.19,31].As catalysts for the formation of higher alcohols, porous $LaCo_{1-x}Cu_xO_{3-\delta}$ (LCCu) perovskite oxides were produced in 2007.In this synthesis process, Elements of Group I was utilized as addictive alkalis, successfully controlling the growth grain of phases of perovskite while acting as a soft template. The LCCu perovskite displayed a large specific surface area and many holes when the alkali (0.08wt% of alkali ions) was washed away in water, indicating increased catalysis activity for high alcohol preparation by syngas. Furthermore, the surface-specific areas of the resultant compound changed with a radius of cationic metals of alkali utilized and the increase is in order of Li < Na (≈ Cs) < K< Rb respectively**.** During the ball milling procedure porous La $Fe_{0.8}$ $Cu_{0.2}O_3$ and $LaCo_{1-x}Fe_xO_3$ were also used as perovskite oxides and was well synthesized in the presence of numerous additives and displayed a higher surface specific area for synthesis which uses convection, diffusion processes, permits for speedy transfer of mass transit in the phase of liquid and allows reactant to mixed on an atom scale [21,36-37]. The salt of a resulting sample could be eliminated by washing it with water that is de-ionized after pyrolysis resulting in porous products.

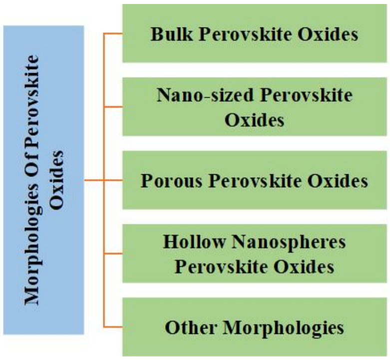

Figure. 1 Perovskite Oxide different structures

The ratios weight of metal salts of alkali (e.g., $ZnCl_2$, NaCl, KOH, and $NaNO_3$) to solid precursors have ranged from 1:1-15:1 in prior investigations [32-40]. According to some experts, a high ratio can aid in mesopores formation [35-40]. As a result, particle size, morphology, porosity, and other parameters may be effectively modified with molten salt. For decades, molten salt synthesis has been effectively utilized to generate perovskite oxides, particularly ferroelectric oxides such as $BaTiO_3$ and $SrTiO_3$ [32]. Furthermore, molten salt synthesis was used to create single-crystalline $BaZrO_3$ particles, allowing for rational control of the structure of perovskite oxides [41]. Aside from these, other perovskite oxides can be made using this process [21, 32-34, 37-39].

Li and his colleagues reported a molten salt solid-state precursor methodology for the fabrication of $LaCoO_3$ perovskite. To conduct the precursor reaction, they mixed solid-state $Co(NO_3)_3.6H_2O$ and $La(NO_3)_3.nH_2O$ with a preset amount of KOH after several hours of calcination nanoparticles in porous form having diameters of 15nm to 40 nm were formed [39]. By significantly altering the calcination period various porous nanostructured $LaMnO_3$ including spheres and cubes were well created employing a co-assisted molten salt method involving $NaNO_3$ and KNO_3 [24]. $LaMnO_3$ took on a porous spherical shape after calcination at 550°C for 4 hours with the pore's mean size of 34.7 nm. SEM and TEM images are shown in Fig 2-(b,c,d,e). After increasing the time of reaction up to 6 hours, reveal single-crystal porous cubic $LaMnO_3$ particles. The production mechanisms of several $LaMnO_3$ nanostructures are prepared as shown in Fig (2-f). XRD pattern of $LaMnO_3$ is shown in Fig (2-g). It was discovered that shape significantly impacted activity in the catalytic elimination of toluene.

Song et al. recently synthesized $La_{0.6}Sr_{0.4}Co_{0.2}Fe_{0.8}O_{2.9}$ porous using a standard molten salt process in which the mixed oxide precursors were combined with a 2:1 weight ratio eutectic salt mixture of NaCl and KCl [21]. Fig (2-h) shows scanning electron microscopy (SEM) pictures of porous nanoparticles interconnected with a macroporous cores diameter of 200 nm. The porous arrangement made a huge interfacial surface, exposing more active sites and even perhaps strengthening OER catalytic activity. When compared to the benchmark IrO_2 precious metal-based catalyst, the $La_{0.6}Sr_{0.4}Co_{0.2}Fe_{0.8}O_{2.9}$ porous catalyst had a lower over-potential of 345mV and a density of current of 10mA cm^{-2} (360mV). Molten salt techniques are also used to make Sr, Mg doping in perovskite form $LaAlO_3$ porous for electrolyte SOFC and $La_{0.8}Sr_{0.2}MnO_3$ perovskite powders for the SOFC cathode [22].

However, according to what has been observed, excellent molten salt synthesis perovskite oxides still make up just a tiny proportion of the whole perovskite oxide group. This could be owing to some variables, including the relatively high temperatures at which phases occur (usually > 1000°C) or the likelihood of molten salt reacting and reactants. Even though most modified solid-state approaches do not involve pore size management, they have been shown to improve the surface area and reduce particle size. Several modified solid-state synthesis methodologies have been utilized to target pure phase formation, controllable particle sizes, and associated specific areas. However, due to the unforeseen and random pore-forming processes, controlling the porosity and/or pore size is difficult. More research is needed to better understand phase formation and pore growth in molten salt synthesis, which would greatly improve the design of porous perovskites for applications such as electro-catalysis [14].

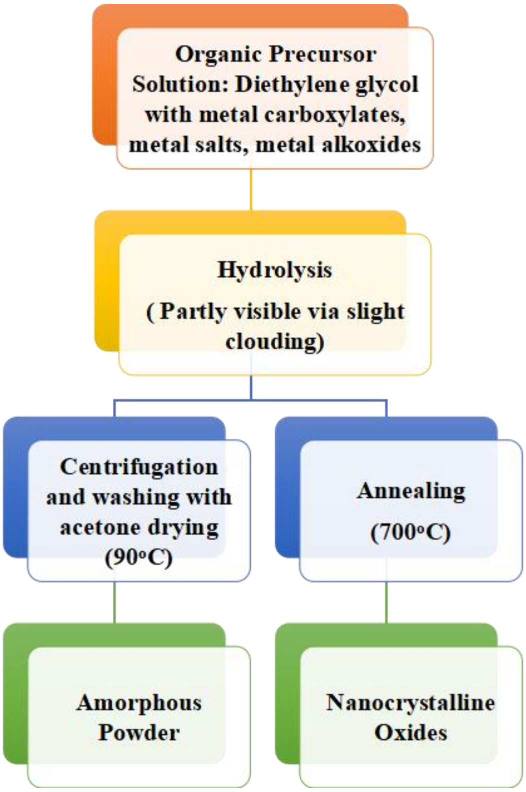

Scheme 1. Synthetic technique for perovskite-type oxides using polyol mediates the synthesis.

2.3.2. Wet Chemical Process

Wet chemical techniques for developing porous metal oxides have been widely used and have made significant progress in recent decades [42-55], while multi-metal oxides still need to be studied further. Porous materials have been developed using surfactants and templates. After the template, the surfactant was removed under mild conditions, and with additional calcination procedures, porous solid material can be well generated [14].

Wet chemical synthetic methods such as the process of sol-gel, methodology of complexation, combustion solution technique, route of hydrothermal, synthesis of electro-spinning, and a few others have been developed. Controlled morphology and porous structures, as well as perovskite oxide nanoparticles, are of particular interest [14,21,54-60].

2.4. Hollow Nano-spheres Perovskite Oxides

Nanospheres with hollow interiors are a newer type of nanosphere. Perovskite has a bigger surface area and energy than mixed perovskite because of its hollow structure, allowing for the doubled face (inner and exterior) interaction with the reactant. Good perovskite oxide performance of catalysis may be achievable as a result. Hollow perovskite is made using a variety of techniques, including One approach for simulating the material using a spherical template, like spheres of carbon [61] or directly synthesizing hollow materials using organic guiding agents and a hydrothermal technique [62,63]. Scheme 2 depicts the synthesis of LCMO nanospheres using template-assisted growth.

The carbon spheres might be made by either exfoliating organic precursors (such as glucose) or replicating hollow perovskite oxides utilizing a silica template, which would be utilized as a template (secondary) to duplicate the hollow oxides of perovskite in the first stage. This image shows the usage of a carbon spheres template with silica as a template secondary for the synthesis of hollow oxides of perovskite [64]. Firstly, sucrose was added to the template of silica, which was subsequently carbonized, to create a carbon-silica composite. The composite of carbon silica etched in the 48% of aqueous HF solution, revealing carbon copy, removal of template of the silica. The pores on the carbon copy were then filled with a pre-prepared solution with the required metal cations. Finally, the mixture was dried and calcined at particular temperatures to achieve the desired result. Zhang et al. [63] suggest a quick procedure. The hydrothermal approach is described in the next paragraphs. The nitrates of metals, citric acid, P123, and urea were initially mixed in ethylene glycol, water, and ethanol. The solution was placed in an autoclave and boiled at about 100°C for 48 hours after which it was completely dissolved. The product solid was centrifuged and dried before being calcined for 8 hours at 600°C in the flow of air to get perovskite oxides.

On the other hand, the carbon spheres template technique necessitates manufacturing carbon spheres before the creation of hollow perovskite oxide, making the process more complicated overall. Because of the homogeneous particle size of the silica template, spheres of carbon, eventually, oxides of perovskite having particle that is uniform in size could be

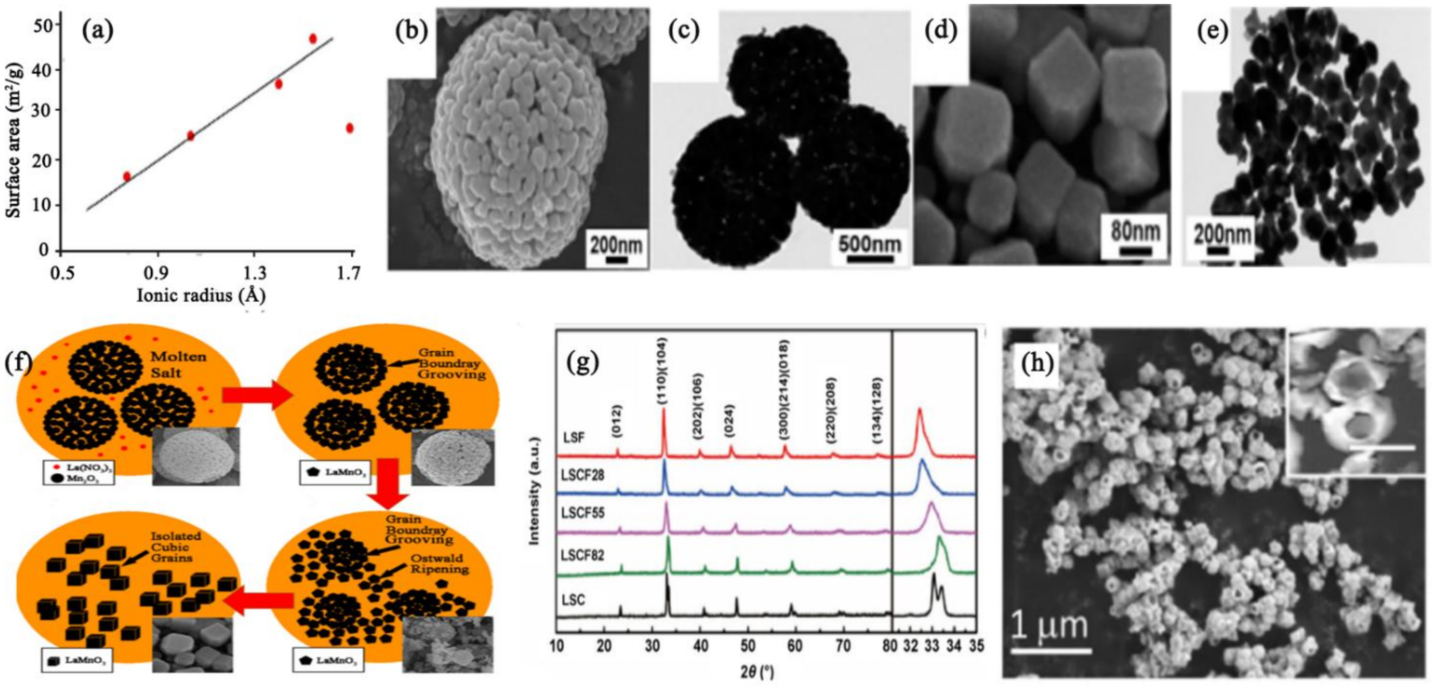

Fig. 2-a) Relation among radius of cationic metal of alkali with a surface area of oxides of perovskite generated. Having the consent of ref. [18] this image has been reproduced. Copyright 2007 Journal of Catalysis b) SEM c) Images showing transmission electron microscopy (TEM) of a porous spherical $LaMnO_3$ sample. d) Scanning Electron Microscopy Analysis and e) Having TEM, porous cubic images of $LaMnO_3$ materials were captured. f) suggested the production process of different $LaMnO_3$ Nanostructures in molten salt media, where the structure of LaMnO3 was modified from porous-cubic nanoparticles. This image has been reproduced with the permission of ref. [24]. Copyright 2014 ACS applied materials and interfaces g) XRD patterns h) SEM images of the synthesized porous nanostructured perovskite LaO.6SrO.4CoO.2FeO.8O_2.9. Inset (h) the equivalent enlarged image. Reproduced from ref. [21]. Copyright 2018 Nano Res.

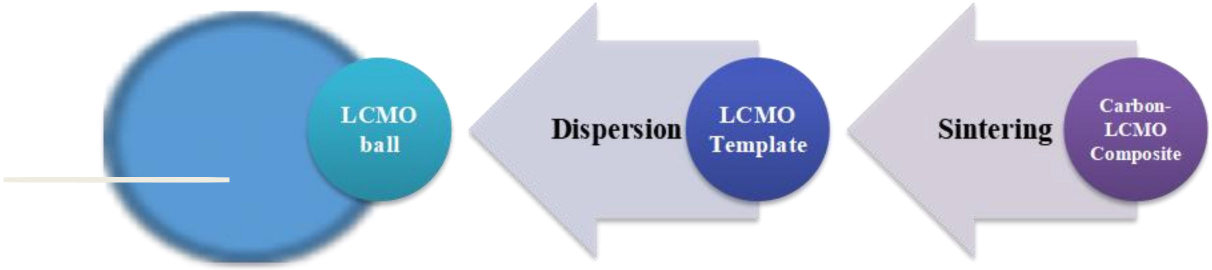

Scheme 2 The creation of LCMO nanospheres using a template-assisted approach is depicted in a series of schematic illustrations [64].

duplicated. Moreover, the particle of perovskite oxides could change from silica to having the required particle size [1].

2.5 Other Morphologies

With the evolution of materials research and the growing need for innovative applications, oxides of perovskite have different techniques, such as nanoporous perovskite oxide, a nanoplate, nanofibers, nanotubes, flower-like, and cubic, have been created. These various morphologies would allow perovskite oxides to have a wider range of surface characteristics and uses. We went over nanoporous perovskite oxides in great depth.

2.5.1. Nanoporous Perovskite oxides

Hard template, soft template, hydrothermal, colloidal crystal template, and electrospinning procedures are some of the most common ways to make nanoporous perovskite oxides. We only go into detail on the synthesis of soft and hard templates and colloidal crystal templates.

(a) Soft-Template Method

Soft templates have been highlighted [65] in the creation of materials of nano-porous like silica of mesoporous like MCM-41 [66], and SBA-15 [67]. One of the most efficient ways to make mesoporous oxides is to use evaporation-induced self-assembly (EISA). Direct co-condensation methods are typically combined with soft templates. The EISA approach has four steps: (a) Synthesis of a homogenous initial sol including the soft templates and inorganic precursors in the proper stoichiometry; (b) During the dip-coating methodology, solvent evaporation caused inorganic precursors to self-assemble into micelles with a poorly compacted network and a steadily increasing strength over Critical Micelle Concentration CMC. (c) Additional inorganic condensation and film equilibration with its surroundings are responsible for the final mesostructured adjustment. (d)Temperature treatment is produced before consolidation, template removal, and chain crystallization. Even though “EISA” technology was utilized to generate mesoporous oxides of single-metal several times, it was only utilized to make mesoporous perovskite oxides a few times. The cations from the first gel mixed homogeneously on a molecular scale throughout the entire procedure to generate mesoporous oxides of perovskite having pure phases. In as-prepared samples, however, variations within the solubility of components that are non-volatile in the evaporation of solvent procedure frequently result in the separation of phase or secondary phases. Furthermore, because the EISA method uses a lower temperature for the breakdown of organic surfactants than for the crystallization of perovskite oxides, mesostructures destroy due to a lack of support at calcination of high temperatures, allowing amorphous phases or impurities to emerge. Despite these difficulties, a few papers have been published on the EISA technique for the preparation of mesoporous oxides of perovskite [68]. In 2004 Grosso and company utilized a semi-commercial template of organic for making mesoporous oxide of perovskite films [68] Brezesinski and company [69] effectively generated many Nano porous oxides of perovskite films with honeycomb 3D structures using the “EISA” technique of associated dip coating onto a polar substrate with several amphiphilic block copolymers with high thermal stability. Although the methodology of EISA, when paired with dip coating can make nanoporous perovskite oxides, it is often challenging and limited to small-scale production. A modified EISA method for manufacturing nanoporous perovskite oxides without the need for precipitants or chelating agents was recently devised by certain researchers which eliminates the necessity for dip-coating. These chelating chemicals would result from the further solution that is homogenous and greater dispersion of cation in the process of evaporation, yet they would have an impact on surfactant self-assembly and interactions with ions of metal. As a result, hierarchically nanoporous perovskite oxides such as $BaTiO_3$, and $SrTiO_3$ may be generated using these improved EISA techniques [70,71].

Because of the great ability of hydrolysis of titanium precursors, there is still much research utilizing the self-assembly of soft template technique for generating higher structured mesoporous oxides of perovskite. $BaTiO_3$ oxide of perovskite having mesostructure inside crystallites was produced directly from solution using the cationic surfactant cetyltrimethylammonium chloride using a simple sol precipitation technique (C16TMAC) [72]. Yan and company developed a higher ordered mesoporous $ZnTiO_3$ with a greater pore volume, a large surface area, and narrow pore dispersion size utilizing the method of sol-gel in combination with EISA with ethanol and F127 Pluronic being structure guiding reagents [73].

(b) Method of Using a Hard Template

Nanocasting, also known as repeated templating, is a process for manufacturing nanostructured materials with unique features. A method employed in this procedure is to fill metal precursors into porous templates made of mesoporous carbon or mesoporous silica, which are subsequently calcined and etched away using acid or alkaline etching [74].

The template of the hard approach utilized to make nano-porous oxides of perovskite for the past decade includes mesoporous $LaNiO_3$ utilizing template SBA-15 and $LaFe_xCo_{1-x}O_3$ utilizing KIT-6. There are several distinctions between hard-template procedures for perovskite and single metal oxides due to the usage of multiple precursors metal for oxides of perovskite. Mesoporous silicas (such as SBA-15, MCM-48, and KIT-6) and mesoporous carbons (such as CMK-3, CMK-1) are frequently used as "hard templates," as seen in [75]. After calcination, agents of Chelating were added to the metal salt precursor solution to obtain a stoichiometrically correct homogenous metal salt precursor solution. When silica is removed with NaOH or HF aqueous solution, mesoporous oxides of perovskite with an organized structure of mesoporous and a high specific surface area are formed. An image of TEM of mesoporous oxide of perovskite is shown in

Because of the complicated interactions between silica and ion of metal precursors filtrated, it can be difficult to fill the mesoporous silica at once, necessitating the observation of a comprehensive impregnation of metal precursors over long periods. Larger oxides of perovskite particles are frequently found outside the pores of mesoporous silica. As a result, various innovative approaches have been devised to increase metal precursor impregnation while reducing external pore loading, such as functionalizing mesoporous silica templates to a group of organic compounds [76]. Similarly, the mesoporous perovskite oxides reported using mesoporous silica as a hard template are confined to little varieties, namely those having composition $LaB_{1-x}B'_xO_3$ (B, B′= Mn, Co, Fe, Ni). Chelating chemicals such as citric acid must be added to metal nitrate precursor solutions to form pure-phased perovskite oxides in lesser calcination temperatures. Another drawback of the hard template method is that correctly draining the silica utilizing a solution of NaOH/HF is difficult, silica residue impacts the hard-characteristic template progress [77]. These issues can be solved by utilizing mesoporous carbon as a template-hard since high-temperature calcination can completely obliterate the carbon template. Based on a silica Aerosil, the process of nano casting in a micro-mesoporous carbon resulted in $LaFe_{1-x}Co_xO_3$ perovskite oxides with a high specific surface area Fig 4(A) [78]. The inorganic precursors are converted into perovskite oxide nanoparticles in the process of calcination at 800°C in air, while the carbon is removed by oxidation. However, there are several drawbacks to employing mesoporous carbon as a template, including inadequate aqueous precursor solution wetting of the pore walls and a low decomposition temperature. Normal impregnation fails to properly fill the pores resulting in perovskite particles developing outside the pores, which is the underlying problem with the hard-template approach. As a result, it will be necessary to build more user-friendly solutions. Due to high interfacial tension in mesoporous structures, the double-solvent method which combines a significant amount of hydrophobic solvent with an aqueous metal precursor solution with a pore volume, may provide an effective method for enhanced metal precursor penetration [79].

The mesoporous structure of $LaFeO_3$ material is shown in Fig (4B). Silica modification of the surface with different groups that are functional on the interior or exterior surfaces will promote metal precursors to be impregnated due to interactions between metal precursors and functional groups [73,80].

(c) Method for Creating Colloidal Crystal Templates

Another typical production method for the crystalline technique uses nano-porous materials of perovskite having 3D organized macro-pores. Inorganic porous materials with sizes of pores ranging from nanometers-micrometers have been successfully produced using organic polymer spheres. Depending on the synthesis approach, three methods for manufacturing periodic structures of macro-porous using a colloidal crystal template are presented in Fig (5) [81]. The vacant gaps between monodisperse spheres packed close together e.g., Polystyrene (PS) or Polymethyl methacrylate (PMMA) and in-situ precursor solidification are filled or covered with liquid metal precursors in these colloidal-crystal-template techniques. The three-dimensionally organized macroporous (3DOM) structures may be made by removing the templates and calcinating them at a high temperature. Inverse opals have a three-dimensional interconnected structure that allows big molecules to move swiftly and gas to diffuse quickly.

Two benefits of employing the template of colloidal crystal technique for generating nanoporous oxides of perovskite are the capacity to manufacture ordered nanoporous perovskite oxides and employing calcination at a high temperature. The 3DOM $La_{0.7}Ca_{0.3}MnO_3$, $La_{0.7}Ca_{0.32-x}Sr_xMnO_3$ was created by Hur et al. [82] by dissolving stoichiometric metal acetates and 2-methoxy ethanol in HNO_3 then gently dumping the thick solution until the millimeter PMMA template was completely immersed. The SEM and TEM images of $La_{0.7}Ca_{0.3}MnO_3$ are shown in Fig (3A, B). Sintering at 800°C in an oxygen environment was used to remove PMMA colloids. On the other hand, making a metal alkoxide solution is labor-intensive and expensive. Using a colloidal-crystal-template technique, researchers created 3DOM oxides of perovskite precursors including solutions of ethylene glycol methanol of different metal nitrates.

Zhao and co-created 3DOM $LaCo_xFe_{1-x}O_3$ perovskite oxide using this method [83]. Various Surfactants of Organic, chelating compounds are utilized to equally distribute nitrates of metal throughout the crystal colloidal template process in the formation of oxides of 3DOM perovskite. Dai and co, for example, employed a surfactant-assisted PMMA templating procedure to make 3DOM $La_{0.6}Sr_{0.4}FeO_3$ with a mesoporous or nano void-like framework, and the findings demonstrated that the nature of the solvent and surfactant affects the surface area and pore structure of the end product [84].

According to researchers processing the $La_{0.6}Sr_{0.4}FeO_3$ a precursor in the development of $La_{0.6}Sr_{0.4}FeO_3$ 3DOM would be favored at 500°C by N_2 for amorphous carbon and so in the air about 7500°C. Dai's group synthesized many types of 3DOM perovskite oxides using citric acid, PEG (Polyethylene Glycol), and triblock copolymer (pluronic P123) including $EuFeO_3$, $Eu_{0.6}Sr_{0.4}FeO_3$, $LaMnO_3$, $La_{0.6}Sr_{0.4}MnO_3$ and La_2CuO_4 [85].

The noble metal nanoparticle-assisted crystal colloidal template approach was used to create 3DOM oxides of perovskite in a single step. 3DOM, for example, supports silver nanoparticles. PMMA was employed as a template in a dimethoxytetraethylene glycol (DMOTEG) solution to generate $La_{0.6}Sr_{0.4}MnO_3$ with larger areas of surface (38.2-42.7 m^2/g), and the DMOTEG-mediated procedure resulted in size-controlled silver nanoparticles that were also stabilized against agglomeration without the need of extra styrene [86].

In a methanol solution by combining stoichiometric quantities of $La(NO_3)_3$, $Pd(NO_3)_2$, and $Mn(NO_3)_2$ with PEG and lysine in an aqueous HNO_3 solution, Wang and co-created a 3DOM Pd-$LaMnO_3$ composite [87]. The 3D porous structure may still collapse or be lost during or after the template removal due to the delicate material nature, which has considerably lower wall thickness than the pore size. As a result, the stability of the pore structure of 3DOM perovskite oxide should be checked frequently throughout manufacture and usage.

Another disadvantage of the crystal colloidal template strategy is the cost and time required to create templates of polymer, which confine the practical applicability of metal 3DOM oxide of perovskite. To generate pure phase 3DOM perovskite oxides, organic matter or detergent must be added to the possibility for molecules that are organically interacting with CCT must be addressed when using a precursor solution of metal ion to evenly divide the ions of metal [73]. Different Synthetic protocols with their corresponding positive and negative aspects are shown in Scheme 3.

3. Methods for Making 1D Perovskite-Type Oxide Nanostructures

In the last ten years, many uni-dimensional oxide nano-structures of perovskite have been produced. The most commonly used techniques are "top-down", and "bottom-up". There are two types of preparation procedures for 1D perovskite nanostructures.

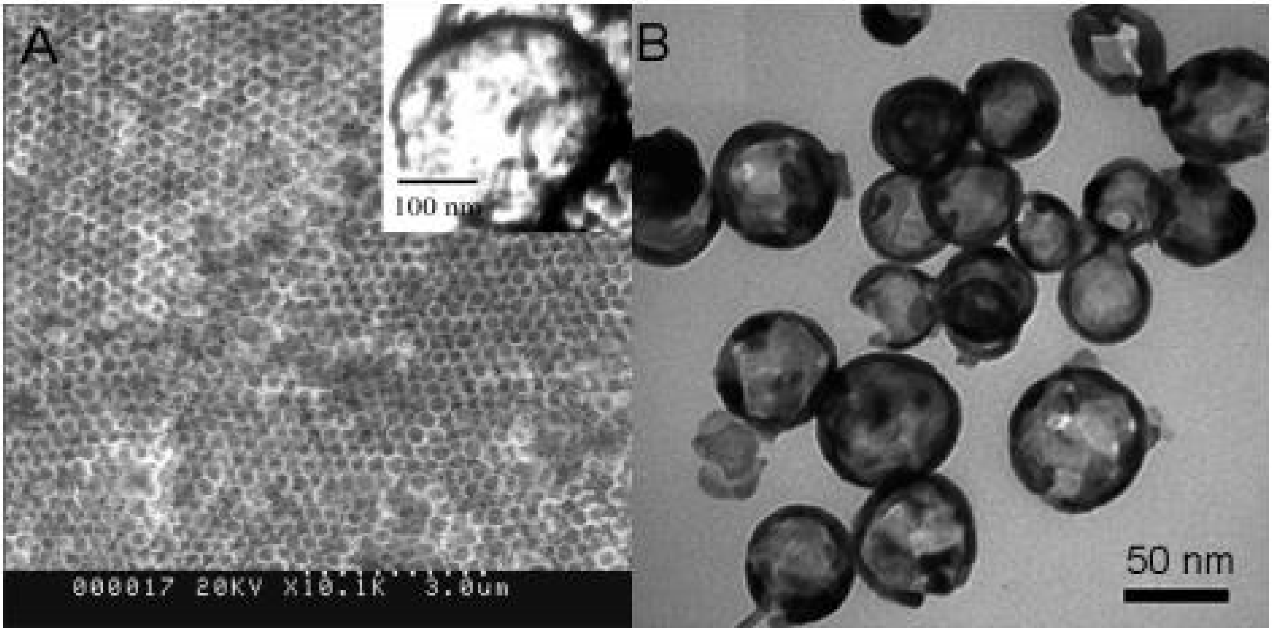

Figure. 3 (A) La0.7 CaO.3 MnO3 spherical array duplicated from the carbon template, as seen in SEM. A TEM picture of a La0.7 Ca0.3 MnO3 sphere with a hollow sphere feature is shown in the inset. (B) TEM picture of hydrothermally produced LaCaMnO3. Reproduced with permission from ref. [1]. Copyright 2014 ACS catalysis

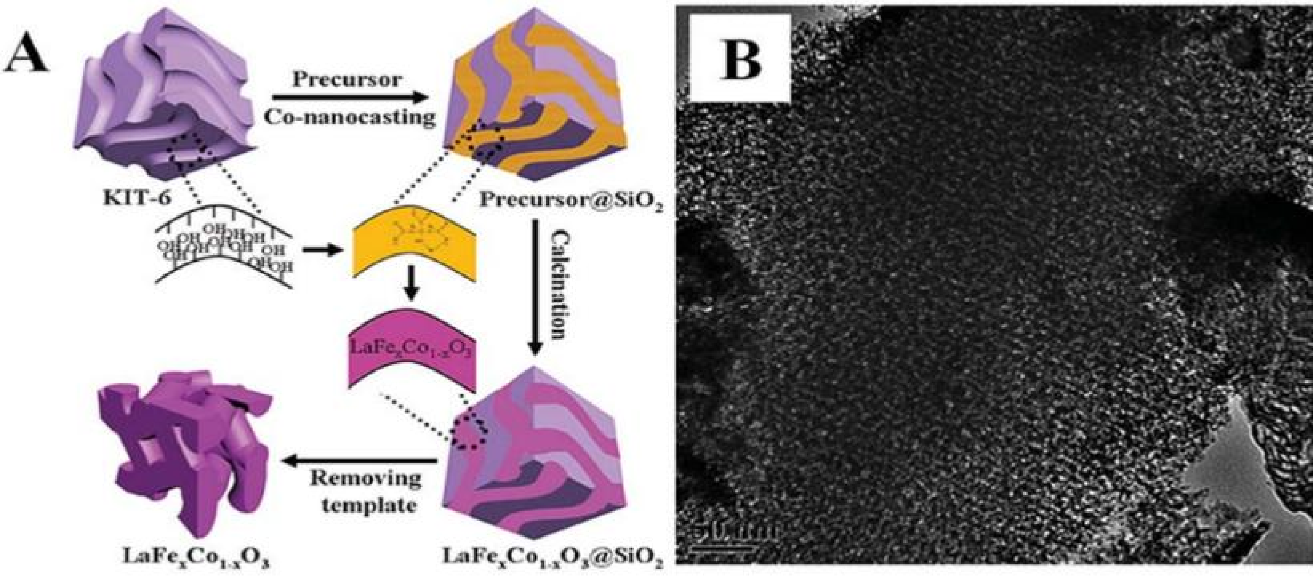

Figure. 4(A) The mesoporous $\mathrm{LaFe_xCo_{1-x}O_3}$ perovskite oxides were made using a co-nano casting process using a rigid template of mesoporous KIT-6, (B) $\mathrm{LaFeO_3}$ that has been developed as a mesoporous material. Reproduced with permission from ref. [73]. Copyright 2018 Chemical Science

The first method does not use a template, but the second does. The following section examines recent advances in manufacturing unidimensional oxide nano-structures of perovskite.

3.1 Template Free Synthesis

Hydrothermal or solvothermal preparation, the salt of molten approach, and the process of electro-spinning having used to build uni-dimensional oxide nano-structures of perovskite without the need for a template.

For example, Joshi and co [88] created perovskite of single crystalline BT ($BaTiO_3$), ST nano-wires using a solution-based approach of free templates. Piezoelectric (PZT) single crystalline nanowires were also made using the template-free hydrothermal method [89]. The templates need not be removed after the perovskite oxide nanowires are generated because this approach does not require organic templates. BT, ST, and PT single crystalline nano-wires are made using the methodology of molten salt. Precursors' surface and interface energies, as well as the molten salts used, are crucial in the synthesis of molten salt nanowires. To make monocrystalline BT nanowires, the metal of alkali titanates is employed as precursors of synthetic in a modified hydrothermal method. Tetragonal Pt uni crystalline nano-wires with a necklace-like shape have also been made via electrospinning. Their lengths range from tens to various tens of micrometers, while their diameter range from 100-200nm. Sol-gel electrophoresis was also used to make tetragonal PZT nanofibers for mechanical energy harvesting nanogenerators [90-92]. Despite its time-consuming and low-throughput nature, the advantage of this technology is that the nanostructures generated can be morphologically controlled. Perovskite nano-tubes' oxides are also made using free template methods like hydro-thermal manufacturing (PONTs). For example, the hydrothermal method was utilized to make BT and BST nanotube arrays on titanium substrates. Constant BT crystalline and ST PONTs were also made employing a low-temperature hydrothermal method using TiO_2 nanotubes as a bonafide precursor material [93-95].

3.2 Synthesis using Templates

The template-assisted approach is an excellent way to mass-produce regular nanostructured arrays in large numbers. The most frequent templates so far have been colloidal monolayers, anodic aluminum oxide, block-copolymers, and nanoimprint molds. Unidimensional oxide of perovskite nano-structures have been created using template-assisted procedures, which have the following benefits: (1) regular nanostructured arrays with a high density; (2) a high surface-to-volume ratio; and (3) finished product dimensions with excellent control over the template channels. With success in the procedure, the oxide of perovskite $La_{0.825}$ $Sr_{0.175}$ MnO_3 nanowires having a polycrystalline perovskite structure was also generated [96,97]. Perovskite oxide nanotubes are created utilizing a sol-gel template-based approach in addition to perovskite oxide nanowires. Hernandez et al. [98] published ground-breaking research using (Anode Aluminium Oxide) AAO templates and the so–gel process to synthesize perovskite $PbTiO_3$ (PT) and $BaTiO_3$ (BT) nanotubes. PZT and multiferroic $BiFeO_3$ BFO nanotubes were made using the same approach. Even though the nano-tubes sizes and shapes can be feasibly controlled through templates, template-based approaches produce polycrystalline nanotubes in general, attributed to nucleation of heterogeneous on walls pore; this process produces tiny uni-crystalline oxide of perovskite nano-tubes. Anti-ferroelectric PZ PONTs were formed utilizing pulsed laser deposition in templates of AAO made up of nanoparticles with diameters ranging from 3 to 7nm and a wall thickness of roughly 10nm. Sol-gel electrodeposition would be utilized to produce PZT nanotube arrays, in which the channels of the templates of AAO are filled with PZT-prepared sol driven from electrophoretic DC voltages. As a result, the filling effect was substantially improved. Manganite nanotube arrays of perovskite were categorized by utilizing microwave irradiation and AAO template-assisted synthesis [99]. This approach allows for the production of arrays of nano-tube at lesser temperatures.

Perovskite $La_{0.59}$ $Ca_{0.41}$ CoO_3 nanotubes are also made using sol-gel templates. A template-inorganic precursor and low-temperature calcination were also used to make perovskite $LaNiO_3$ nanotubes [100]. $LaNiO_3$ nanotubes have a polycrystalline structure with very tiny crystals ranging in size from 3–5 nm [95].

4. 2 D Perovskite-Type Oxide Nanostructure Preparation Methods

Thin-film, arrays of nano-dot, lamellae patterns, nanosheets, nanoplates, and nanowalls are only a few examples of perovskite oxide 2D nanostructures essential in today's microelectronics. As a result, numerous methods for generating perovskite oxide 2D nanostructures have been discovered in the last few years. This section discusses the two-dimensional perovskite ferroelectric nano-structures oxide based upon planar-structures and oxide of perovskite nanosheets, as well as oxide of perovskite thin films and multilayers.

4.1 Multilayer Perovskite Oxide Thin Films

The process that transforms the gaseous state of atoms, molecules, or ions into substrate films or multilayers is known as the oxide of perovskite thin film or multilayer growth. For growing oxide of perovskite thin-films/multilayers, PVD physical vapor deposition methods like PLD, magnetron-sputtering RF, and chemically methodologies like CSD, CVD, and MOCVD, as well as MBE, are all commonly used methods (MBE). This section briefly discusses PLD, CSD, CVD, MOCVD, as well as MBE.

4.2 Laser Deposition using Pulses (PLD)

Smith and co initially used the PLD approach to create dielectric thin films in 1965 [99] and it has since become a prominent thin film growth method. The capacity of the PLD technique to yield film compositions that are almost equal to those of the target, despite the target's complicated stoichiometry, is its most crucial property. Several thin films of oxide of perovskite or multi-layers are generated by altering the PLD process parameters. The literature has an excellent review of the epitaxial development of thin films oxide of perovskite and super lattices.

4.2.1. Chemical Solution Deposition

Because of its low cost, ease of setup, and ability to coat large areas, Chemical Solution Deposition (CSD) is a promising approach for generating thin films. It was first developed for the oxide of thin films of perovskite in the mid-1980s. To date, the CSD method has been used to make a large number of oxide of perovskite thin films. Four processes are involved in the production of oxide of perovskite thin films: Preparation of the precursor solution, spin coating/dip-coating of solution on the substrate, deposited solution of pyrolysis in lesser temperatures, and high-temperature crystallization of the films [101-103].

4.2.2. Chemical Vapour Deposition (CVD) & Metal Organic Vapour Deposition (MOCVD)

CVD is a widely used method for producing high-quality and performance thin films of perovskite oxides across a vast area (CVD).The synthesized materials must have a high vapor pressure when used as a precursor in the CSD process. The substrate compulsorily increases temperature to a specific temperature to improve the reaction's deposition and adatom mobility. To successfully install complicated multi-component thin films oxide of perovskite with homogenous compositions across a vast region, the utilized precursors must have matching thermal properties and acceptable vapor pressures. Improved film quality control has been accomplished using modified CVD methods based on liquid or aerosol generation injection. Liquid injection CVD was used to deposit PZT perovskite, lanthanum-barium-manganite ($La_{1-x}\ Ba_x\ MnO_3$) thin films, whilst aerosol and plasma-assisted CVD was used to create $La_{1-x}\ Sr_x\ MnO_3$ perovskite thin films [104].

Perovskite oxide thin films and super lattices are made using metal-organic chemical vapor deposition (MOCVD). Improved film stoichiometry control, greater crystallization quality, and the ability to cover complicated structures and wide areas are just a few of the benefits of this procedure over standard physical deposition methods. Some of the MOCVD variants that have been developed to satisfy a range of applications include MOCVD at low pressures, MOCVD at atmospheric pressures, MOCVD with direct liquid injection, and MOCVD with plasma enhancement. In the MOCVD injection process, the creation of micro-droplets of solution of the precursor is controlled with a high-speed electro valve pumped in the system of the evaporator. The injection frequency and timing are used to change the optimal growth rates of different deposited materials. Injection MOCVD is now being utilized to produce ferroelectric oxide of perovskite thin films including Barium strontium Titinate (BST), PT, PZT, and BFO, as well as oxide of perovskite super lattices like $(BT/ST)_n$ & $(LSMO/STO)_n$ [105].

4.2.3. Molecular-Beam Epitaxy (MBE)

In the same way that atomic spray painting employs alternatively shuttered elemental sources to maintain cation stoichiometry carefully, the MBE process for producing perovskite oxide thin films uses alternatively shuttered elemental sources to produce high-quality perovskite oxide thin films. Major problems in MBE multicomponent oxide synthesis in only a few applications include regulating oxide substrates terminated at well-defined ionic planes and monitoring the deposition of individual molecular/atomic layers. Reflection high energy electron diffraction) RHEED is frequently utilized for in situ monitoring of the developing surface in MBE. MBE has previously been utilized to fabricate high-quality thin-films oxide of perovskite and epitaxial heterostructures [95].

5. Planar Perovskite Oxide Nanostructures in 2 Dimensions

5.1 Top-Down Methods

A diversity of "top-down" 2D perovskite oxide nanostructured materials based on planar topologies have been constructed thus far using methodologies such as transmission electron microscopy, electron beam lithography (EBL), and nanoimprint lithography (NIL). Alexe and his colleagues were the first to construct a slightly elevated ferroelectric memory based on multiple perovskite ferromagnetism oxide nanostructure formations. Regular arrays of $SrBi_2 Ta_2O_9$ & PZT nanoisland capacitors with lateral dimensions less than 100 nm were safely manufactured using the EBL procedure. After the BT nanodots were cut from the BT single crystal using Focused Ion Beam FIB technology, the zone structures inside the BT dots were evaluated [95,106].

5.2 Bottom-up Methods

Bottom-up techniques, including syntax synthesis, have been employed to create two-dimensional oxide of perovskite nanostructures based on lateral arrays of nanodots in addition to top-down solutions. Using template-assisted "bottom-up" synthetic technologies, nanosphere lithography was applied to produce BT, PZT, and $SrBi_2Ta_2O_9$ ferroelectric oxide nanodots with narrow size and distribution. Lee et al. [107] utilized ultrathin AAO membranes as a stencil mask and PLD method to build PZT arrays on Pt/ MgO substrates. Ultra-high density ferroelectric memory might be allowed by Pt/PZT/Pt nano-capacitors with a density of 176 Gb/inch^2 [95].

6. Methods for making 3D Oxide Nano-structures of Perovskite-Type

Both "bottom-up", and "top-down" methodologies can be employed to create 3D nanostructures. "Top-down" nanostructure production options include using FIB technology to cut away bulk ferroelectric material and construct logically and continuously ordered nanosized structures. Exact placement and effective control over the shapes and sizes of the nanostructures formed are two major advantages of using "top-down" methodologies for FIB milling to make 3D perovskite oxide nanostructures. On the other hand, the FIB milling machine has a range of negative effects, including slower milling and patterning frequencies, thus causing difficulties for volume patterning nanostructures, specifically bigger ones [108].

Furthermore, difficulties have occurred at the nanoscale as a result of impact ions causing damage to the sample surfaces. Because the features of 3D oxide of perovskite nanostructures are highly influenced by their morphologies and ordered alignments, large-scale nanostructure arrays with the required shape and structure are important. A glass substrate, electron

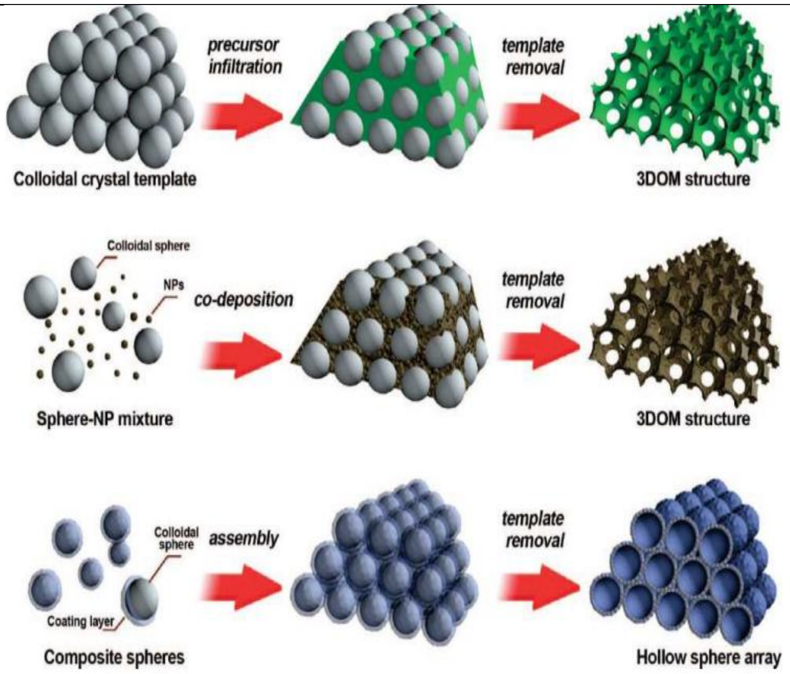

Figure. 5 Three colloidal-crystal-template methods for producing periodic macroporous structures. Top: Precursor material is infiltrated into a preformed colloidal crystal, which is then treated to generate the 3DOM structure once the template is removed. Middle: To make a 3DOM structure homogenous, once the template is removed the nanoparticles (NPs) and templating spheres are co-deposited. Bottom: Hollow shells are produced by regularly arranging core-shell components. This diagram has been reproduced with the permission of ref. [73]. Copyright 2018 Chemical Science

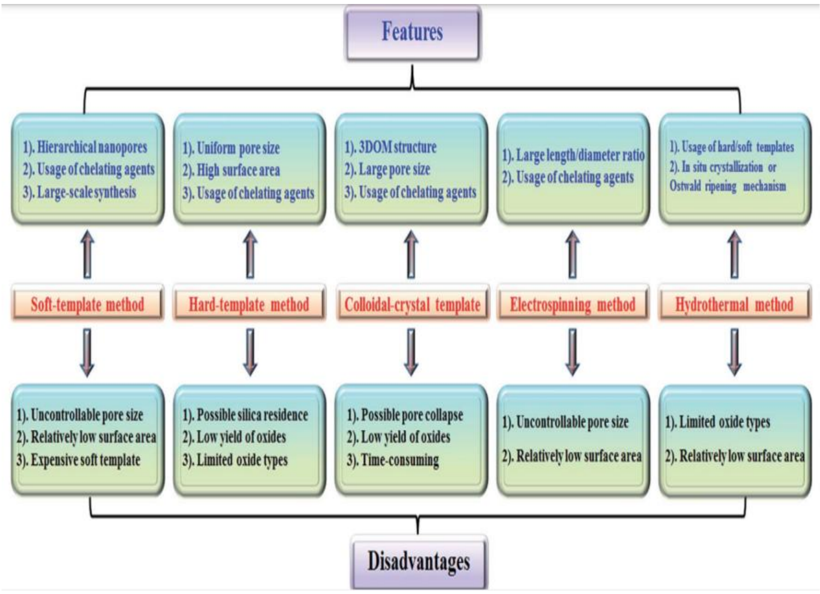

	Soft-template method	Hard-template method	Colloidal-crystal template	Electrospinning method	Hydrothermal method
Features	1). Hierarchical nanopores 2). Usage of chelating agents 3). Large-scale synthesis	1). Uniform pore size 2). High surface area 3). Usage of chelating agents	1). 3DOM structure 2). Large pore size 3). Usage of chelating agents	1). Large length/diameter ratio 2). Usage of chelating agents	1). Usage of hard/soft templates 2). In situ crystallization or Ostwald ripening mechanism
Disadvantages	1). Uncontrollable pore size 2). Relatively low surface area 3). Expensive soft template	1). Possible silica residence 2). Low yield of oxides 3). Limited oxide types	1). Possible pore collapse 2). Low yield of oxides 3). Time-consuming	1). Uncontrollable pore size 2). Relatively low surface area	1). Limited oxide types 2). Relatively low surface area

Scheme 3 Synthetic approaches for nanoporous perovskite metal oxides are summarized from ref. [73].

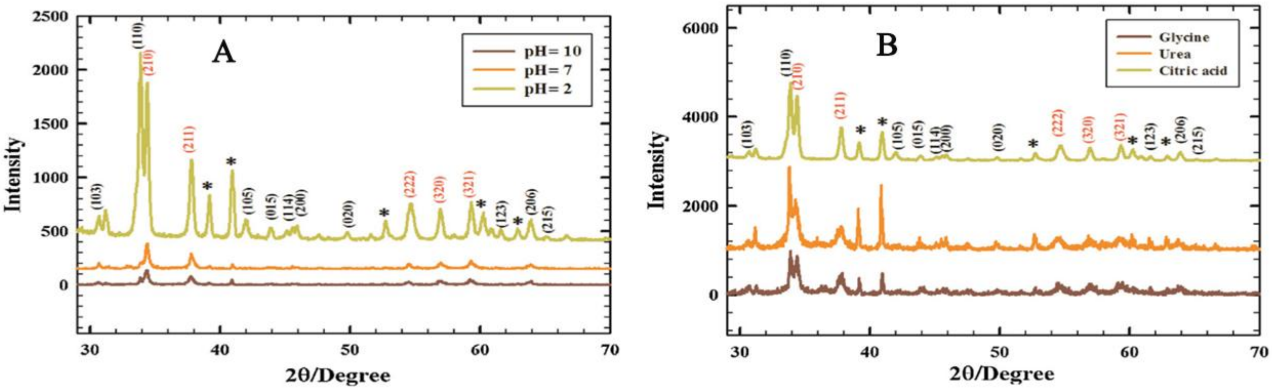

Figure. 6 Patterns of XRD of SrPdO3 created from a combustion process at varied pH levels (A) for various fuels (B) SrPdO3, SrPd3O4, and SrCl2. Miller indices (h, l, k) are given in black for SrPdO3, red for SrPd3O4, and the sign (*) for SrCl2... Reproduced with permission Ref. [110]. Copyright 2014 Electrochimica Acta

Table 1. Lattice parameters of $SrPdO_3$ synthesized by different methods

	Lattice Structure	**Particle Size (nm)**	**Lattice Parameters (A)**	**Lattice Volume (A^3)**	**Theoretical Density (g/cm^3)**
Standard $SrPdO_3$ (ICCD card, 00-025-0908)	Orthorhombic		a=3.977 b=3.350 c=12.82	179.98	4.47
Citrate-nitrate method	Orthorhombic	34.0	a=3983 b=3.541 c=12.80	180.59	4.45
Urea-nitrate method	Orthorhombic	45.4	a=3.954 b=3.563 c=12.82	180.63	4.45
Glycine-nitrate method	Orthorhombic	25.7	a=3.972 b=3.527 c=12.83	179.69	4.47

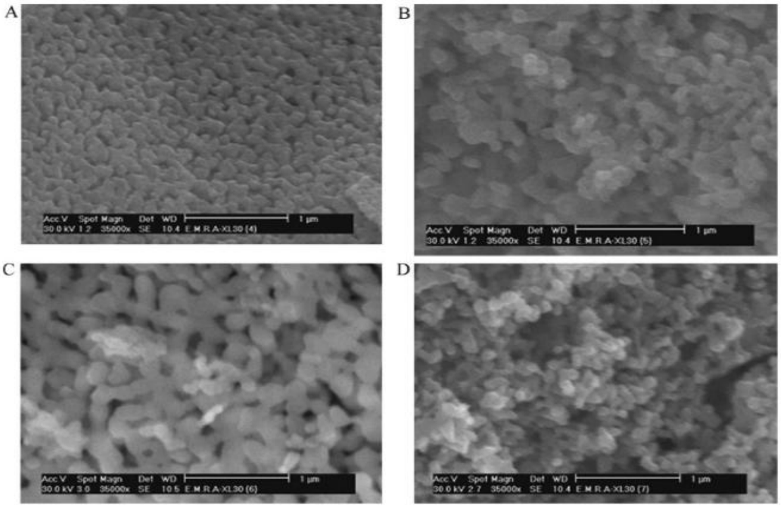

Fig. 7 Images showing SEM analysis of **(A)** ‘$LaNiO_3$’**, (B)** ‘$LaCoO_3$’, **(C)** ‘$LaFeO_3$’ and **(D)** $LaMnO_3$ was produced using a microwave-assisted citrate technique at 720W for 30 minutes, magnified 35,000 times. From ref. [112]. Copyright 2014 Electrochimica Acta

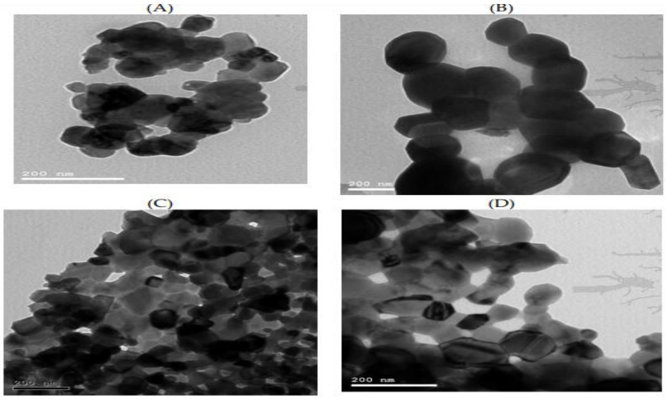

Figure 8. Images showing HRTEM analysis of **(A)** ‘$LaNiO_3$’, **(B)** ‘$LaCoO_3$’, **(C)** ‘$LaFeO_3$’, and **(D)** For 30 minutes, microwave-assisted citrate was employed to generate $LaMnO_3$ @ 720W. according to the source ref. [111]. Copyright 2008 Journal of magnetism and magnetic materials

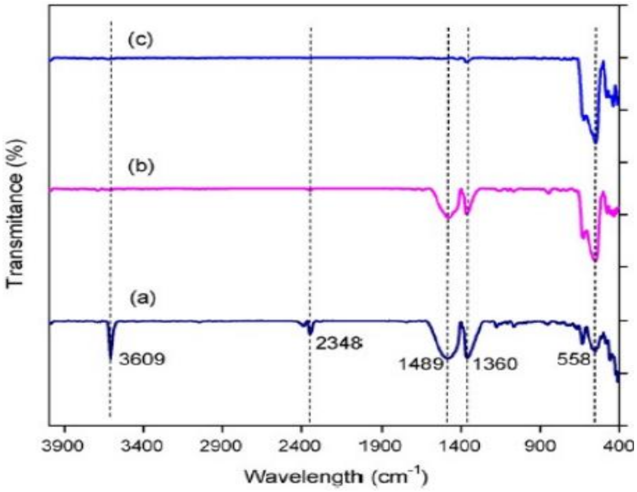

Figure. 9 FTIR spectra of $LaFeO_3$ produced with permission From ref. [113]. Copyright 2008 Bulletin of materials sciences

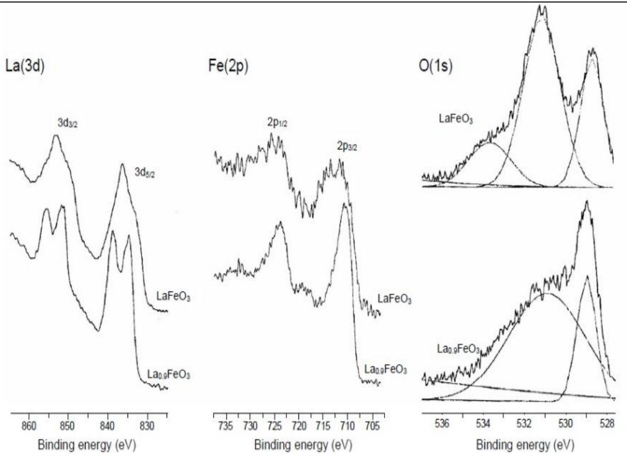

Figure 10: La (3d), Fe(2p), and O(1s) XPS spectra in $La_{0.9}FeO_3$ and $LaFeO_3$ samples. From ref. [114]. Copyright 2009 Bulletin of the Korean chemical society

beam lithography, and scanning probe lithography are used to achieve results [95].

7. Perovskite Characterization

The distinct phases of the perovskites generated may be distinguished by X-ray powder diffraction (XRD). Another approach for determining the structure of perovskites is single-crystal XRD. Thermal analytic techniques such as TGA, DTA, and DSC can be used to study the thermal stability of the produced perovskites. SEM & TEM, on the other hand, may disclose a variety of structural and surface properties of the perovskites created [109]. We chose a variety of perovskites from earlier research as examples for characterization investigations in this study.

7.1. $SrPdO_3$ perovskite

a. XRD

Galal et al. [109] Fig. (6A) show the XRD patterns of $SrPdO_3$ synthesized at pH values of 2, 7, and 10 for 3 hours at a calcination temperature of 750 °C. The Intensified Charge Couple Device (ICCD) results for $SrPdO_3$ were compared to those of the XRD. The real and theoretical pH 2 values are very close. This helps form the primary orthorhombic phase of perovskite of $SrPdO_3$ (major diffraction peak 110) and the secondary phase of $SrPd_3O_4$ emerged (210). In prepared samples of pH 7 & 10, only the $SrPd_3O_4$ phase was visible, while the (110) peak vanished. XRD patterns of $SrPdO_3$, $SrPd_3O_4$, and $SrCl_2$ are shown in Fig (6B).

Consequently, the optimal pH for generating $SrPdO_3$ is pH 2. XRD may also be used to optimize the kind of (citric-acid, urea, and glycine) $SrPdO_3$ made with this material. In all cases, $SrPdO_3$ was the dominant phase, albeit with differing percentages of $SrPdO_3$ (110) compared to $SrPd_3O_4$ (210). The proportion was greater in the case of urea, but low in the case of citric acid. Table 1 lists the structural parameters that were calculated as well as well-matched theoretical data [109].

b. SEM and TEM

Perovskite nanoparticles' morphology and physical features may be explored using SEM and TEM. The SEM of the formed perovskites was strongly influenced by the preparation environment, synthesis methodology, types of A- & B-site ions of metal, and doped A- and/or B-sites. Galal and co. [109] employed 720W as the working power for 30 minutes of microwave irradiation to synthesize $LaNiO_3$, $LaCoO_3$, and $LaFeO_3$ are all oxides of nickel, cobalt, iron., and $LaMnO_3$ using the microwave-assisted citrate technique.

The SEM images of several perovskites i-e$LaNiO_3$, $LaCoO_3$, $LaFeO_3$, $LaMnO_3$ are displayed in Fig (7). $LaNiO_3$ had a surface as compact with a greater degree of order, whereas $LaCoO_3$ and $LaMnO_3$ had spherical grain agglomerations with smaller grain sizes in $LaMnO_3$ and greater grain sizes in $LaCoO_3$ and $LaMnO_3$, respectively. $LaFeO_3$ has a unique shape, with a porous surface filled with bonelike particles. $LaFeO_3$ has greater electro-catalytic activity than other perovskites in the hydrogen evolution process [109].

In addition, HRTEM may demonstrate the various morphologies and particle properties of several perovskites [111]. HRTEM images of $LaNiO_3$, $LaCoO_3$, $LaFeO_3$, and $LaMnO_3$ were prepared using the microwave-assisted citrate technique Fig (8). Images of $LaFeO_3$ taken using HRTEM revealed a crystallinity-rich orthorhombic phase, whereas $LaNiO_3$, $LaCoO_3$, and $LaMnO_3$ HRTEM photos revealed hexagonally deformed rhombohedral phases. For the different perovskites, the HRTEM diffraction patterns were similar to the XRD data [109].

c. FTIR

The perovskites' chemical bonding and chemical structure that has been generated may be investigated using FTIR. In the same way that XRD may provide structural evidence, the FTIR can as well. Biniwale et al. [113] synthesized $LaFeO_3$ using various methods, including sol-gel, combustion, and co-precipitation. In the FTIR of $LaFeO_3$, the stretching vibration mode of Fe-O was detected as an absorption band at 558cm^{-1} Fig (9). The O-Fe-O vibration mode was discovered to be linked to the 430cm^{-1} band. In $LaFeO_3$, which is connected to La-O in lanthanum oxide, co-precipitation produced a strong band at 3609 cm^{-1}. The band at 3600 cm^{-1} simply vanished in the other two methods, suggesting the production of a somewhat pure perovskite phase. Additional bands occurred at 1360 and 1480 cm^{-1} in the co-precipitation technique, indicating future stages. Consequently, the absorption peak of about 558 cm^{-1} was connected to metallic oxygen bond stretching modes, as described in the literature [109].

d. XPS

The surface compositions of the individual components of the developed perovskites may be examined utilizing XPS. Lee et al. [114] prepared $La_{0.9}FeO_3$ and $LaFeO_3$ samples and investigated their structural composition using XPS analysis. Fig (10) exhibits the XPS spectra of La (3d), Fe (2p), and O (1s) in $La_{0.9}FeO_3$ and $LaFeO_3$ samples. The binding energy of La ($3d_{5/2}$) in $LaFeO_3$ and $La_{0.9}FeO_3$ was 833.5eV and 833.8eV, respectively, corresponding to the La^{+3} ions in the oxide state. In both samples, however, the bandgap of Fe ($2p_{3/2}$) was 710.2 eV. This signifies Fe^{3+} ions in the form of oxide. The Fe (2p) XPS signal can't understand the difference between Fe^{3+} and Fe^{4+}. The XPS signal of O (1s) was split into two peaks at 529.9 and 532.1 eV in the case of $La_{0.9}FeO_3$. The O (1s) XPS signal for $LaFeO_3$ contained three peaks: 529.4, 531.9, and 534.4 eV. The binding energies of O (1s) at lattice oxygen species are 529.9 and 529.4 eV in both experiments. The chemisorbed oxygen species OH or O are important for the peaks at 532.1 and 531.9 eV. The binding energy of chemisorbed oxygen species is 2.1– 2.5eV bigger than even lattice oxygen species. In the instance of $LaFeO_3$, the peak at 534.4eV was ascribed to adsorbed water species related to the particularly hygroscopic surface lanthanum oxide [114,109].

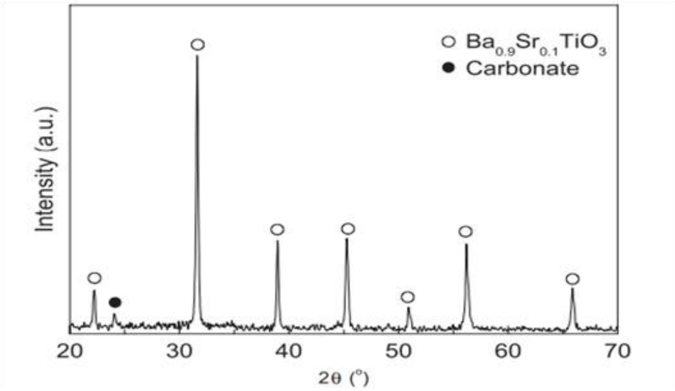

Fig. 11 ($Ba_{0.9}$ $Sr_{0.1}$) TiO_3 nanoparticles X-ray diffraction pattern. Reproduced with permission from ref. 115. Copyright 2005 Journal of solid state chemistry

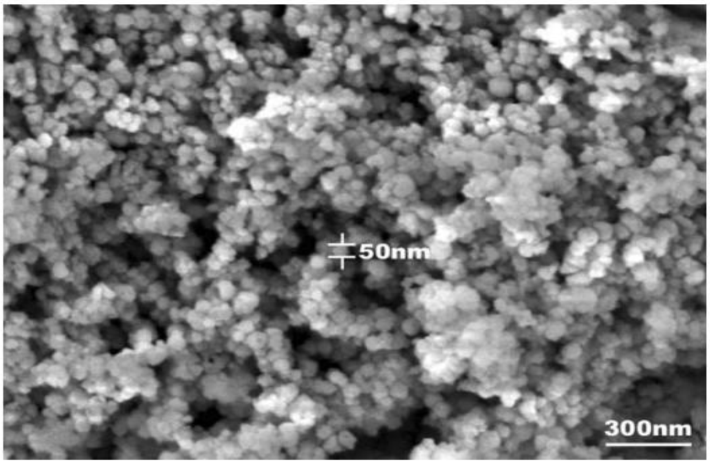

Figure 12: Using field-emission scanning electron microscopy, BST nanoparticles were observed (FE-SEM). With permission from ref. 115. SThis article has been reprinted. Copyright 2005 Journal of solid state chemistry

7.2. [(Ba, Sr) TiO_3] Perovskite barium strontium titanate nanoparticles

a. XRD

Jian Quan qi et al. [115] used wet chemical synthesis at room temperature and ambient pressure to make perovskite barium strontium titanate nanoparticles (BST). Starting ingredients include titanium alkoxide and alkali earth hydroxides, which are processed using very simple methods. Changing the processing conditions can change particle size and crystallinity. The crystallinity and phase of the Ba, Sr) TiO_3 nanoparticles were determined using X-ray diffraction. Fig (11). In the XRD pattern, at 24^0 barium carbonate appears as a peak. The interactions between carbon dioxide dissolved into solutions from the air and alkaline earth hydroxides are proposed to be the reason for barium carbonate manufacturing. Finishing the production in a protected climate (such as argon or nitrogen) or scrubbing the powders with dilute acids can prevent the impure phase [115].

b. SEM, TEM

The microstructure of as-produced particles of BST was further described using SEM and TEM shows a typical SEM picture of the synthesized BST nanoparticles. The particles are homogeneous in size and have a diameter of 50 nm as shown in Fig (12) [115].

The findings of the TEM observation are shown in (The size of the particle found by TEM was 50nm diameter, Fig (13a) which was consistent with the SEM findings. SAED pattern having atom planes of indexed shown in the inset of HR image of TEM is shown in Fig (13b). The image's darker half shows well-organized patterns, indicating that the particles under investigation have solidified. The structural information of the nanoparticles was obtained using a rapid Fourier transform technique, as illustrated in the Fast Fourier Transform (FFT). The material's lattice parameter was discovered to be 0.398 nm Fig (13c). In the FFT image, dislocations were also discovered in Fig (13 d). The production of dislocations is caused by the low synthesis temperature [115].

7.3. Perovskite oxide $Ba_x Mn_{1-x} O_3$

a. XRD

$Ba_xMn_{1-x}O_3$ oxide of perovskite is a good material for producing electrochemical instruments or devices because of its attractive chemical and physical features. Using a hydrothermal technique, Muhammad Rafique et al. [116] synthesized Ba-doped MnO_3 ($BaMnO_3$) with variable Ba concentrations. X-ray diffraction was used to characterize the generated material.

Fig (14) exhibits XRD patterns of $Ba_xMn_{1-x}O_3$ (x = 0.1, 0.15, 0.2), which reveal angles with miller indices of 27.20 (101), 31.60 (110), 380 (002), 41.280 (201), 50.450, 52.90 (211), 560 (300), 65.50 (220), 710 (203), 72.20 (311), and 78.90 (222), respectively. With a = 5.6720, b = 5.6720, and c = 4.7100, hexagonal crystalline structure is discovered. Peaks blue-shift as doping levels rise, with the full width at half maximum (FWHM) increasing and peak strength dropping, reflecting a drop in crystallinity. Doping raises the cell volume and material density to 131.23 cm^{-2} and 6.06 g/cm^{-3}, respectively, after doping. The EDX results reveal that the samples are pure because there are no impurity peaks in the spectra. The crystallite size was calculated using Debye Scherer's formula based on the obtained data [116].

$$D = \frac{K\lambda}{\beta Cos\Theta}$$

CLK = 0.15418nm is the X-ray wavelength, is the FWHM, and is the diffraction angle. K is the form factor (0.9 for hexagonal structures), D is the crystallite size, and CuK = 0.15418nm is the X-ray wavelength. The crystallite size in pure material is 22.1nm. However, when the number of dopants increases, it shrinks. The crystallite diameters of 10wt percent, 15wt percent, and 20wt percent doped $BaMnO_3$ are 21.2, 16.5, and 11.3 nm, respectively. Lattice distortion is caused by a mismatch in the radius of the matrix and the dopant element, which causes crystallite size to decrease. A stress or strain field is created due to this occurrence, disrupting crystal formation in one direction. Because the dopant (Ba) is big, compression forces produce blue shifting of the diffraction peaks. Tensile strains, on the other hand, move the peaks toward larger angles

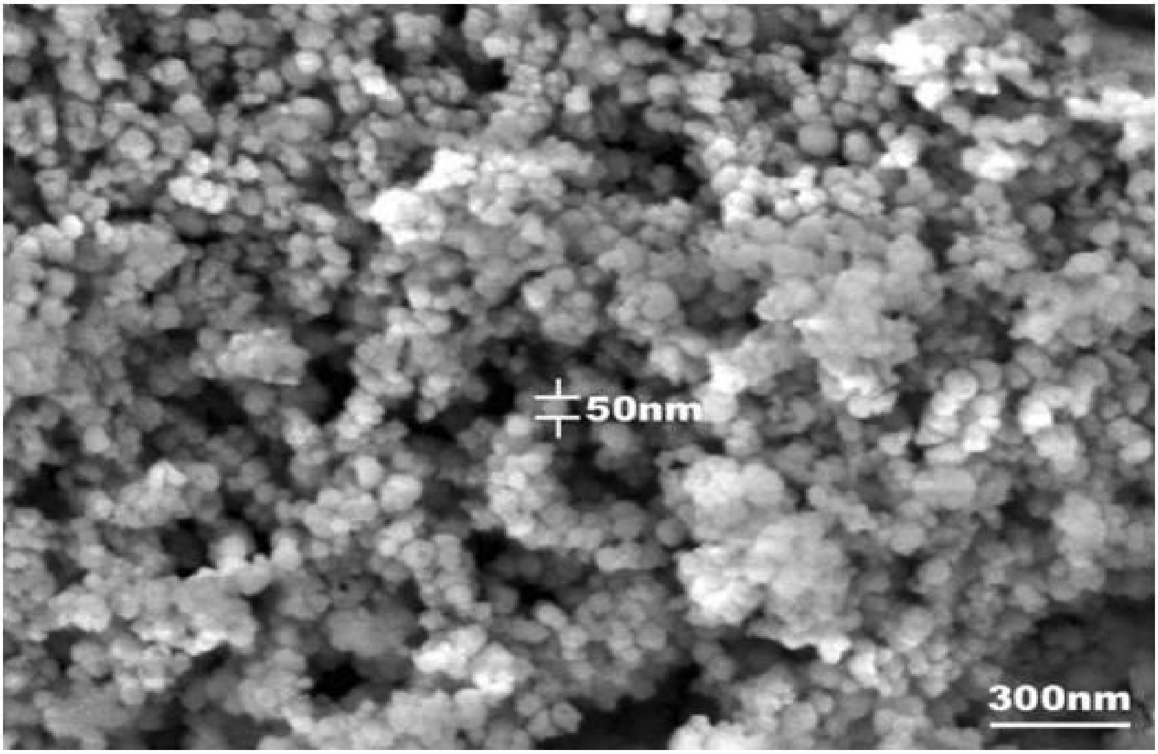

Figure 12: Using field-emission scanning electron microscopy, BST nanoparticles were observed (FE-SEM). With permission from ref. 115. This article has been reprinted. Copyright 2005 Journal of solid state chemistry

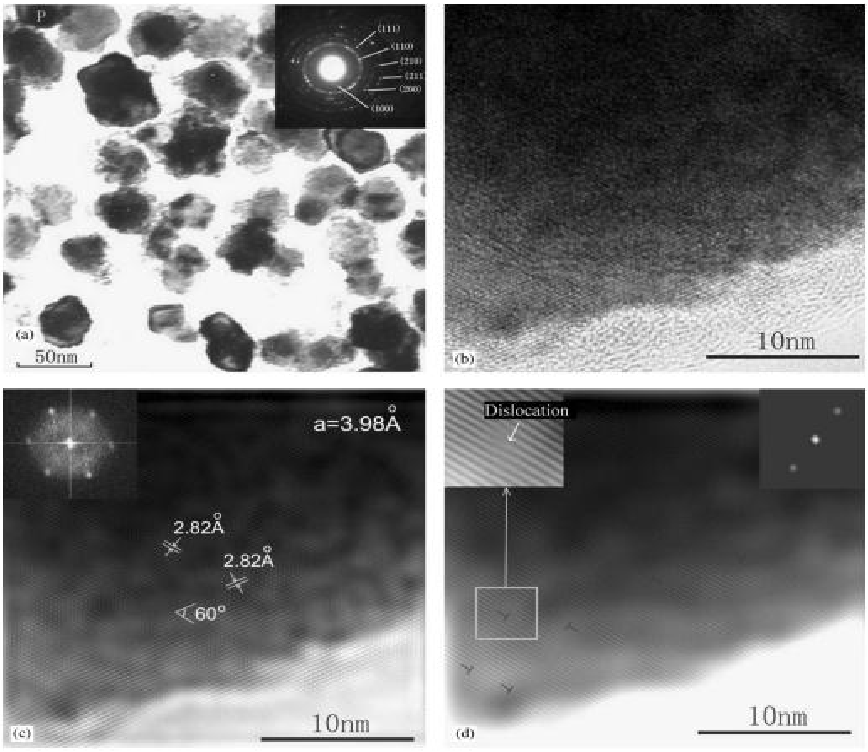

Fig. 13 TEM images of BST nanoparticles**: (a)** 'morphologies'**, (b)** 'HR image', **(c)** This FFT graphic shows the link between the atom planes and **(d)** The dislocations in the nanostructure are seen in this FFT image. Reproduced with permission from ref.

115. Copyright 2005 Journal of solid state chemistry

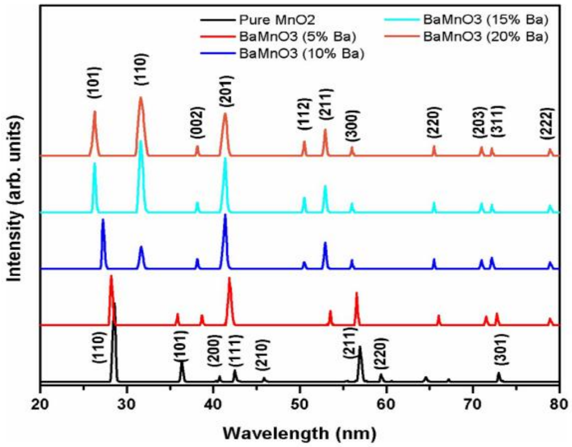

Figure. 14 XRD of pure MnO_2 and 10, 15, and 20wt% doped $BaMnO_3$. Reprint with permission from ref. 116. Copyright 2021 International journal of energy research

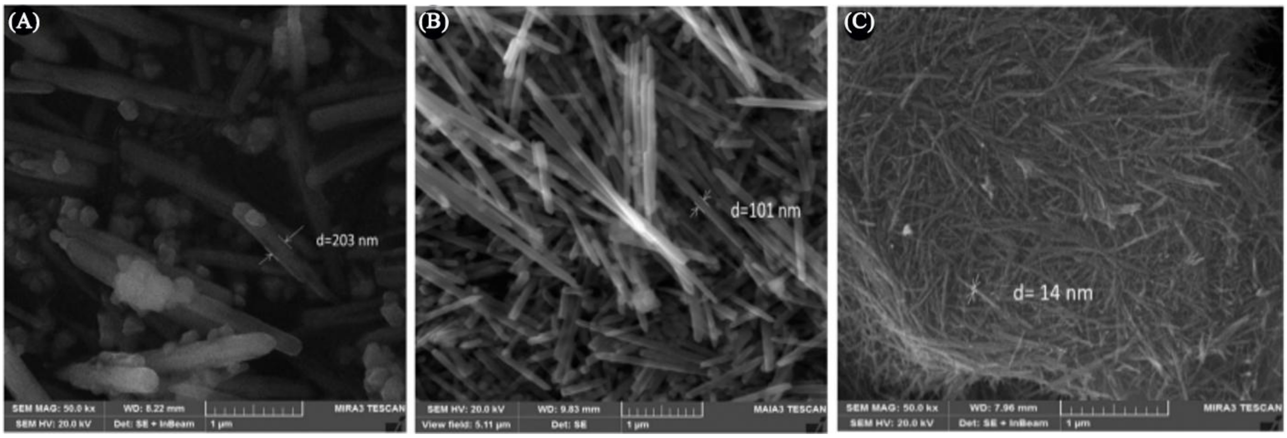

Figure 15: SEM micrographs of Ba_xMnO_3 **(A)** At 10wt% doped $BaMnO_3$, **(B)** At 15wt% doped $BaMnO_3$, and **(C)** At 20wt% doped $BaMnO_3$. Reproduced with permission from ref. 116. Copyright 2021 International journal of energy research

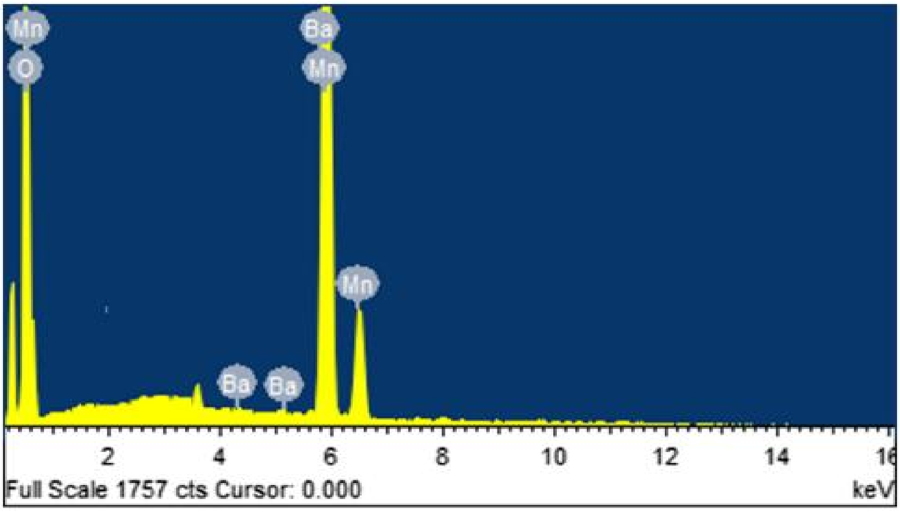

Fig 16: EDX spectra of $BaMnO_3$. Reproduced with permission from ref. 116. Copyright 2021 International journal of energy research

Due to a large amount of dopant. Oxygen vacancies have an important role in structural mobility. A cation vacancy is created in this situation by giving dopants (Ba) an excess positive charge. When these vacancies come into contact with oxygen vacancies in MnO_2, they become less mobile [116].

b. SEM

SEM micrographs of Ba-doped MnO_3 at 10, 15, and 20% by weight are depicted in Fig (15A, B, C). The micrographs for 10, 15, and 20wt percent doped materials reveal nanorods with diameters of 90-110nm, 180-220nm, and 10 to 15nm, respectively [116].

The degree of doping in the nanorods determines their shape and diameter. This is owing to a difference in the materials' ionic radius, which induces bond constriction and, as a result, a size reduction. According to the findings, doping increased the material's surface area, which improved the electrochemical characteristics of MnO_2 by increasing the material's reactive sites [116].

c. EDX

The EDX spectrum of Ba-doped MnO_3 is shown in Fig (16). The spectrum reveals that the samples produced are fully contaminant-free. This spectrum contains only the elements Mn, Ba, and O, contributing 26.45, 7.13, and 65.76 percent by Weight, respectively. As a result, the hydrothermal technique synthesized morphological materials that were both pure and controlled [116].

7.4. $NdNiO_3$ Perovskite Nanoparticles

a. XRD

To create $NdNiO_3$ perovskite nanoparticles that were calcined at various temperatures, M. I.Maulana et al. [117] employed sodium hydroxide as a precipitating agent and polyethylene glycol as a surfactant in a co-precipitation approach.

$Nd(NO_3)_3 + Ni(NO_3)_2 + 5NaOH \longrightarrow Nd(OH)_3 + Ni(OH)_2 + 5NaNO_3$ **(1)**

$2Nd(OH)_3 + 2Ni(OH)_2 \longrightarrow Nd_2O_3 + 2NiO + 5H_2O$ **(heating stage 1) (2)**

$Nd_2O_3 + 2NiO + ½ O_2 \longrightarrow 2NdNiO_3$ **(heating stage 2) (3)**

The products are identified using X-ray diffraction Fig (17). Shows the material's pattern of XRD obtained during manufacturing, calcined at different temperatures. As calculations temperature grew, peaks strength changed. In products of as-synthesis calcined at about 900°C, a crystalline phase of $NdNiO_3$ nanoparticles, ABO_3 perovskite-type, was identified (P900). Peaks corresponding to novel oxide phases ascribed to extraordinarily strong peaks such as Nd_2O_3, NiO, and Nd_2NiO_4 were also discovered at that temperature.

The hydroxide and oxide phases coexist in the calcined synthesis result at 700°C, namely $Nd(OH)_3$, $Ni(OH)_2$, Nd_2O_3, NiO, and Nd_2NiO_4, were formed (P700). The metal hydroxides were expected to not entirely dissolve to oxides during heating step 1 (Reaction 2).However, they can be converted to perovskites at extremely high calcination temperatures. It might be because the first heating stage is just 1hour long. At temperatures below 900 °C, $NdNiO_3$ nanoparticles do not form. Analysis of XRD indicated that P900 was far superior to P700 due to the development of perovskite and the lack of hydroxide compounds [117].

b. FTIR

The materials were analyzed using FTIR before and after calcination. It was done to see if we successfully eliminated contaminants containing undesirable functional groups. It was also hoped that a wide range of vibrations of Ni–O stretching and O–Ni–O bending would be detected. After calcination, the functional groups OH, CH, and CO in the nitrate ion as precursors, NO, and O–H, C–H, and C–O as a surfactant in PEG 400, OH, CH, and CO, should evaporate. It was considered that the substance was pure since it lacked specific functional groups. The PEG structure is shown in Fig (18) [117].

The spectrum of FTIR of PEG 400 as well as the final product before and after calcination are shown in Fig. (19). The spectra of PEG were given peaks of absorption for OH wide stretched, CH stretched, CO stretched, and CO stretched (primary alcohol) vibrations at 3432, 2866, 1092, and 1066 cm^{-1}, respectively. As the temperature of calcination increased, the OH vibrations of stretching were slowly lost and may not be recognized in spectra of P900, & also as on CH stretched and CO stretched vibrations [117].

Oxides of metals, like Ni–O, show absorption peaks under 800 cm^{-1} because of interatomic vibrations. Significant absorption is about 6–7 hundred cm^{-1} region because of Ni–O vibration stretching mode [118].

The peak of absorption at 634 cm^{-1} is also caused by the MO, OMO, and M-O-M (M=Ni, Co) [119] vibrations. According to the FTIR spectrum, Ni–O's stretching vibrations were identified before and after calcination in the product. The stretching Ni–O led $Ni(OH)_2$ to form in the precipitate of the product before calcination. O–H stretching was measured during that time, which supported the idea even more. P700 contains a trace quantity of $Ni(OH)_2$ as evidenced by mild stretching O–H and NiO_2 vibrations in Nd_2NiO_4 compounds. On the other hand, the O–Ni–O vibration in P900 created $NdNiO_3$ perovskite nanoparticles. XRD examination verified that all of these assignments gave $NdNiO_3$ [117].

7.5. $LaNiO_3$ perovskite oxides

a. XRD and SEM

Harikrishnan and co-presented a co-precipitation technique for synthesizing $LaNiO_3$ nanoparticles, which were then annealed at various temperatures. Materials' structure and morphology are studied using XRD Fig (20a) [120]. XRD is utilized to identify the structure of the crystal.

The sample that was annealed at 600 degrees had a less crystalline XRD pattern. The crystalline structure of the $LaNiO_3$ nanoparticles matches 34-1028 which corresponds to a rhombohedral perovskite structure when annealed at temperatures of 700, 800 and 900 degrees Celsius, as illustrated in (Fig. 21) (a) peaks at 23.42°, 33.02°, 40.88°, 41.33°, 47.04°, 53.72°, 54.04°, 58.96°, 59.72°, 68.8°, 69.17°, 74.52°, 78.67°, 79.49° correspond to (101), (110), (021), (003), (020), (211), (113), (122), (220), (029), (303), (312), (214). No other peaks at 700oC, 800oC, or 900oC could be attributed to La_2O_3 or other phases indicating the presence of single-phase $LaNiO_3$ in the sample. The powerful diffraction patterns confirm the material's crystalline structure [120]. The surface morphology of the generated different $LaNiO_3$ (LNO) nano-particles ie LNO1, LNO2, LNO3, LNO4, and LNO5 is investigated using SEM. Fig. (20 b,c,d) depicts the SEM images of the samples. The diverse morphologies of the particles for various calcination temperatures are readily seen in these SEM images [120]. Typically, they appear as a clump of deformed sphere-like particles. Additionally, as the calcination temperature rises, so does the degree of particle agglomeration. Particle grain growth during high-temperature calcination might cause the degree of agglomeration [120].

8. Catalytic Applications of Perovskite Oxides

Oxides based on perovskite having common formula ABO_3 have effectively ammonia oxidation, methane combustion, catalyzed hydrogenation, and CO oxidation, among other reactions. We used examples from previous research that revealed catalytic behavior in numerous conversions to show case the catalytic applicability of perovskite oxides.

8.1. Comparison of Catalytic Activity of $GdAlO_3$, $SrMnO_3$, $SrCoO_3$, and $MnFeO_3$ Perovskite Oxides

Perovskite oxides, which appear to be potential catalysts, appear to enhance VOC combustion. During the combustion method of Propane, benzene, acetone, and gasoline (Pb-free), Nicolae Rezlescu et al. [121] compare the catalysis activity of several ordinary perovskites having variable cationic concentrations. Nanometer particles with nominal compositions of $SrMnO_3$, $GdAlO_3$, $MnFeO_3$, and $SrCoO_3$ were created using the self-combustion sol-gel process and subsequently heat treated in the air at 1000^{o}C. As for catalytic studies, the catalytic activity level varied significantly depending on the perovskite content. $SrMnO_3$ is the most active of the four perovskites when the weather is cold only in the conversion of acetone did catalysts $MnFeO_3$ and $SrCoO_{3-x}$ exhibit considerable activity as catalysts [121].

(a) Perovskites' Catalytic Activity

Perovskites catalytic capabilities in the combustion of investigated (distinct VOCs) at temperatures ranging from 20 to 550^{o}C. For each perovskite composition, Fig. (21) displays the gas conversion as a parameter of reactive temperature. The following considerations should be taken into account: [121]

- The catalytic activity of the perovskite catalyst is affected by the reaction temperature. Raising the reaction temperature aids gas combustion.

- Perovskites of diverse compositions have dramatically different catalytic activity, which is consistent with Seyfi et al findings [122]. Strontium manganite catalyst has higher catalytic activity than gadolinium aluminate catalyst Fig. (21 a,b) The activity differential between the two samples cannot be explained by their different surface areas. The surface area of $GdAlO_3$ is 10 m^2/g, while the surface area of $SrMnO_3$ is 2.2 m^2/g.
- Gas combustion over the $SrMnO_3$ catalyst began at substantially lower temperatures (about100°C) than over other perovskites. The $SrMnO_3$ catalyst's increased VOC conversion activity reflects the existence of reactive oxygen species on the catalyst surface. Because of the high concentration of Mn^{4+} ions on the perovskite surface, oxygen may be less anchored and thus more available for VOC oxidation.
- An interesting result was found for manganese ferrate ($MnFeO_3$) Fig. (21c) and strontium cobaltite ($SrCoO_{3-x}$) Fig. (21d). Regardless of chemical composition, the two catalysts only demonstrated high catalytic activity for acetone conversion and low catalytic activity for propane, benzene, and gasoline catalytic combustion. The reasons for such a restricted catalytic activity are unknown. This behavior could be explained by a rearrangement of their lattice structure, which controls their catalytic properties, and, as a result, the active site configuration. It's worth noting that temperature significantly impacts acetone conversion over the $MnFeO_3$ catalyst. The acetone conversion started at a low temperature (150 °C), and when the temperature increased from 200 to 300 ^{0}C, the conversion rate increased substantially from 10% to 80%. (Fig.22c) This effect was not observed with the other perovskites. Unlike the $MnFeO_3$ catalyst, the $SrCoO_{3-x}$ catalyst started converting acetone at about 200°C and reached an acetone conversion rate of 80 percent around 450°C. The four gases were converted more efficiently using the $GdAlO_3$ and $SrMnO_3$ catalysts [121].

Table 2 shows the data gathered in flame-less combustion of VOC on the four perovskite catalysts. The conversion against temperature graph can be used to calculate T_{10} and T_{50}, which are the temperatures required to convert a gas by 10% and 50%, respectively. T_{50} is a common metric for assessing the catalytic activity of a catalyst [121].

The catalytic activity for complete gas oxidation is sufficient at T_{50} temperature, and there is substantial contact between the catalyst surface and the reactants. The catalyst is more active if this number is lower.$SrMnO_3$ appears to be more active than the other catalysts. It has much lower T_{10} and T_{50} temperatures than the other catalysts [121].

a Reaction rate for VOC concentration at low conversion per unit surface area of catalyst.

b Apparent activation energy for low conversions

The chemical composition of catalysts of perovskite, as well as the kind of used gas, have a very much impact on the performance of the catalyst in the combustion of VOC, as shown in Fig (22). On the other hand, $SrCoO_3$ and $MnFeO_3$ catalysts favor acetone oxidation alone. At 500 degrees Celsius, catalysts can convert 85% of acetone, but only 30 percent of the other gases. In light of the contrast, despite the little surface area, the most preferred catalyst among the four perovskite samples, $SrMnO_3$, has the greatest catalytic activity at low temperatures. This catalyst converted 95 percent of propane, 83 % lead-free gasoline, and 75 percent acetone at 500 Celsius. $SrMnO_3$ less specific area perovskite does not appear to play a role in the catalyst's greater activity. The greater activity of the catalyst to $SrMnO_3$ might be attributable to the increased oxygen mobility generated by vacancies of oxygen caused by the manganese ions' presence of varied valence. The different activity of catalysts of the four perovskites is not able to be described by distinct surfaces. No indication that activity and surface area were linked. Factors like structural flaws and oxygen mobility are likely to affect the catalytic efficacy of these perovskite catalysts [121].

8.2. Methane Oxidative coupling, ABO_3 perovskites are used

Yujin Sim et al. [123] investigated the active-sites behavior of catalysts of perovskite in the coupling that is oxidative coupling/reaction of methane (OCM) utilizing 10 different ABO_3 types catalysts of perovskite) with different structural features based on their A and B site components. In addition to being the structure definite and simple having the stability of heat, these materials offer remarkable activity of the catalyst in a range of conversion of CH_4 activities. According to findings, the surface lattice of catalyst species of oxygen is required for targeted methane conversion. Oxygen species of the surface lattice with lesser binding energies were used to purposefully speed the generation of hydrocarbons of C_2 from the OCM. Oxygen-adsorbed of surface and mixed oxygen lattice species were used to fill oxygen surface gaps created by the interaction of oxygen lattice with CH_4. The oxygen ion conductivity of perovskites is significantly related to this oxygen cycle, which can be predicted using structural features tolerance factor and particular free volume are two examples. The simple oxygen cycle converted a considerable amount of CH_4 during this reaction. Finally, they discovered that the oxygen lattice characteristics and for the systematic design of effective catalysts OCM, the conductivity of ion of oxygen of perovskite catalysts is a major component that influences catalytic activity and must be carefully managed [123].

According to the researchers, the conductivity of oxygen-ion of catalysts of perovskite might be utilized to forecast CH_4 conversion during the OCM process. Higher binding energies lattice oxygen species aided CO generation. Furthermore, the oxygen surface adsorbed species formed by gas-phase oxygen adsorption changed CO_2 to CO.As a result, the electrical characteristics of the oxygen species lattice and the conductivity of oxygen ions are essential determinants in the determination of the OCM activity of the catalyst of perovskites. Under the specified reaction conditions, the catalyst $CaZrO_3$ having strong conversion CH_4 and C_2 selectivity produced the maximum yield of C_2 (14.2 percent) [123].

8.3. $BaCe_{1-x}Mn_xO_{3-\delta}$ perovskite for methane combustion

The Maganese doped in $BaCeO_3$ catalyst oxides of the series composite were synthesized using a sol-gel methodology. According to Xihan Tan et al. [124] methane as catalyst activity of combustion of $BaCe_{1-x}Mn_xO_{3-\delta}$ catalytic oxide of the series composite was investigated on lesser temperatures using a reactor of fixed bed (200-600 °C). Physically catalyst parameters are described using SEM, size of particle analysis, XRD, and measurement of a surface-specific area, while sample conductivity is determined using the impedance of AC spectroscopy [124].

According to the findings, the catalyst oxide of the perovskite phase composite constructed using the sol-gel catalyst phase of perovskite created has excellent catalyst performance and great thermal stability. Catalyst catalytic performance is affected by its conduciveness, which has a proportion in connection. According to the findings, the catalyst oxide of the perovskite phase composite is effectively manufactured using the sol-gel method. The catalyst phase of perovskite generated has better performance and great thermal stability. Catalyst catalytic performance is affected by its conduciveness, and there is a proportional relationship between the two. When the temperature is below 650°C, Mn doping considerably increases the activity of catalysis of the catalyst $BaCeO_3$ for the combustion of methane. As the quantity of Mn-doped rises, the catalytic activity increases at first, then decreases [124].

They also observed that when the sintering temperature climbed, sample conductivity increased firstly then decreased, grew continuously while increasing temperature test, and rose first and then plummeted as the Mn percentage increased. A $BaCe_{0.6}Mn_{0.4}O_{3-\delta}$ catalyst sample sintered at 1250°C had the maximum conductivity at 800°C, 0.4975scm^{-1}. They observed that the conductivity change rule is precisely opposite that of the activation energy in the diagram of Arrhenius of Mn sample conductivity. The activation energy is lowest when the catalyst sample reaches its maximum conductivity. The result of the activity of catalytic oxidation of CH_4 tests explains adding a catalyst considerably enhances methane catalytic oxidation efficiency when compared to doing so without one, and that

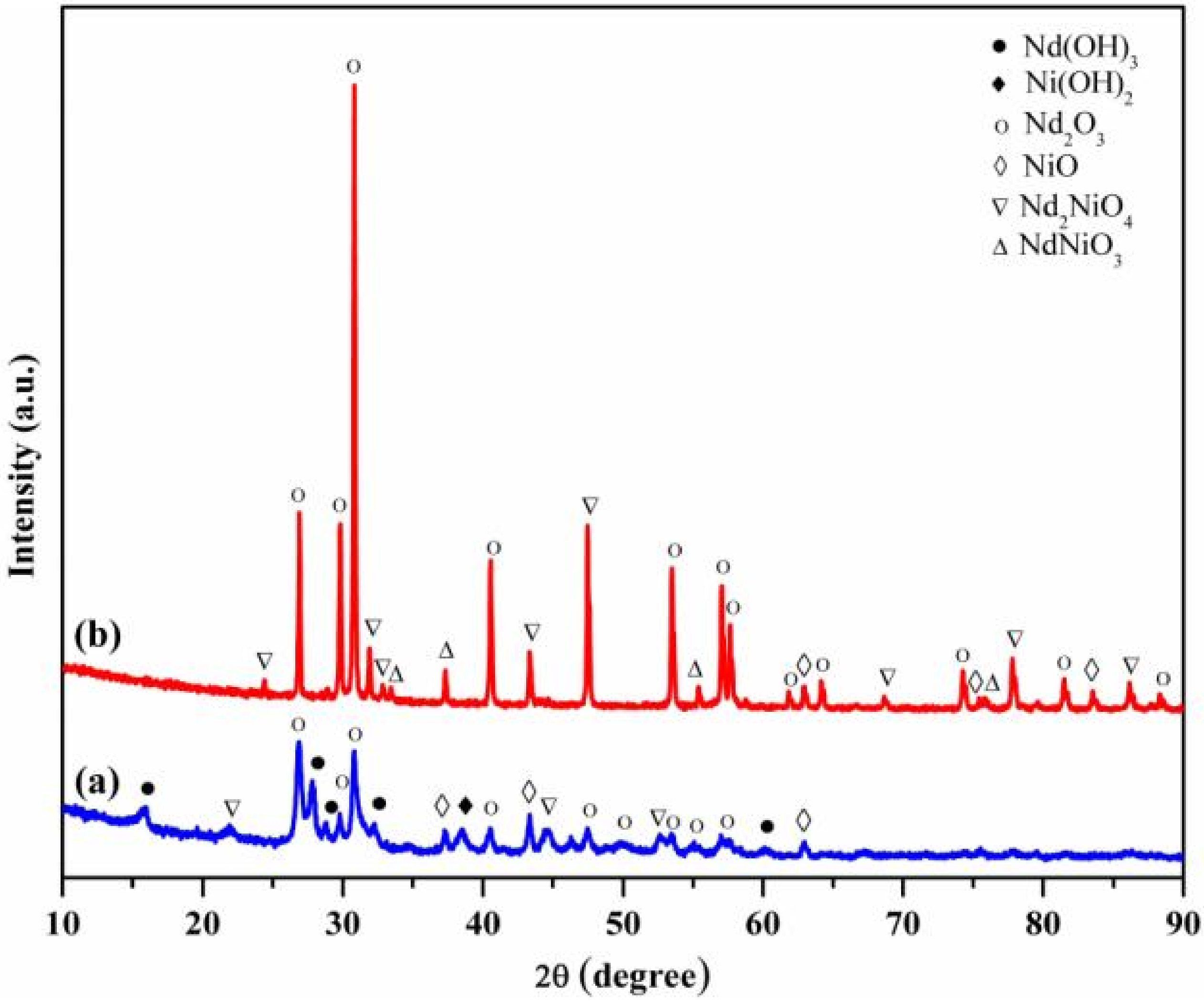

Fig. 17: XRD pattern of calcined materials $Nd(OH)_3$, $Ni(OH)_2$, Nd_2O_3, NiO, and Nd_2NiO_4 during synthesis. Reproduced with permission from ref. [117]. Copyright 2020 Nano Express

CH_4 after doping has a better catalytic oxidation efficiency than $BaCeO_3$. When the element Mn=0.4 is doped, sample catalytic activity peaks of CH_4. The initial temperature of methane is 249.7 degrees Celsius, which is 400.3 degrees Celsius lesser than the experiment of blank, 95.3 degrees Celsius lesser to $BaCeO_3$ [124].

8.4. $Co_xFe_{1-x}O_y$ catalyst for CO_2 hydrogenation

The study of CoO_x–FeO_x catalysts reveals a lot about how multi-transition metal oxide catalysts are made and used. Minshan Meng et al. [125] stated that an efficient and solid-state mechanochemical redox process for obtaining $Co_xFe_{1-x}O_y$ from $CoCl_2.6H_2O$ and $KMnO_4$ was established with just two rounds of ball milling (BM). The transition metal oxide $Co_xFe_{1-x}O_y$ generated in the RWGS method may be used as a high-activity catalyst as well as a CO selectivity catalyst. Over the whole temperature range, selectivity is greater than 80%. At 500 degrees Celsius, it converted CO_2 at a rate of 43 percent, compared to 15.6 percent for $Co_xFe_{1-x}O_y$ -CP and 15.8 percent for $Co_xFe_{1-x}O_y$-SG [125].

During 120 hours of high ambient temperature, the conversion rate of $Co_xFe_{1-x}O_y$–BM increased, suggesting that adding Fe to the Co element improved thermal stability. In the future, such a breakthrough is predicted to be the road to a greater and more efficient system of industries for synthesizing multi-transition metal oxides that are solvent-free and have outstanding catalytic performance [125].

8.5. $La_{1-x}Sr_xCuO$, CO_2 hydrogenation to methanol catalysts

Because it is a cost-effective solution to the environmental greenhouse gas problem, CO_2 catalytic hydrogenation of the methanol process has become a popular CO_2 consumption technique. Structured materials of perovskite have come as very attractive other possible standard catalysts supports for this process because of their mobility of oxygen feature and feasibility of structural increasing adsorption CO_2 capacity by easy having metal oxides of alkali doping. The impact of the adsorption strength of CO_2 on hydrogenation of CO_2 on the activity of methanol in $La_xSr_{1-x}Cu_{1.o}O$ materials with a perovskite structure was investigated and published by Antonius Jeffry Poerjoto et al. [126] $La_{0.9}Sr_{0.1}CuO$ beat all other Sr-modified catalysts in terms of conversion of CO_2 (8.59%), selectivity of methanol on 300°C, 3.0MPa pressure (49 percent). Moreover, $La_{0.9}Sr_{0.1}CuO$ demonstrated sustained catalytic activity over 24 hours with no carbon generation throughout the CO_2 hydrogenation cycle. XRD analysis revealed the forming structures of perovskite in catalysts of calcined. According to XPS research, $La_{0.9}Sr_{0.1}CuO$ has a larger number of lattice oxygen species than the others. Furthermore, because there is a relationship between lattice oxygen concentration and methanol yields, lattice oxygen species are significant for improving methanol selectivity during CO_2 hydrogenation. $La_{1-x}Sr_xCuO$ catalysts of perovskite having catalytic concentration $La_{0.9}$ $Sr_{0.1}CuO$ outperformed another catalysis for hydrogenation of CO_2 in methanol [126].

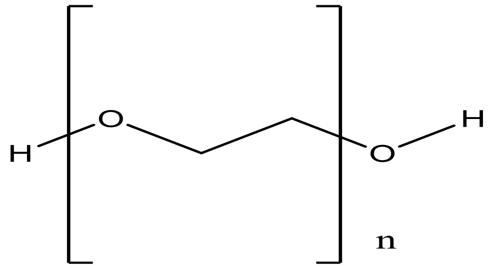

Fig. 18: Polyethylene glycol's chemical structure

8.6. Metal Catalysis on Perovskite-Type Oxides

Rojas Cervantes and colleagues investigated the use of catalysts of perovskite oxide-based oxidation for wastewater treatment using various oxidants and so UV-visible irradiation producing photocatalysis [127]. The researchers investigate the physicochemical aspects of perovskite oxides like lattice oxygen vacancy and mobility formation as well as maintaining distinct states of oxidation of component elements which may be used to increase AOP employing radicals [128].

Using X-ray absorption spectroscopy, Kim et al. [129] show how Fe drives the oxygen evolution process (OER) in the $PrBaCo_{2\,(1-x)}Fe_{2x}O_{6-\delta}$ layer double perovskite used as a catalyst under alkaline circumstances. In $PrBaCo_2O_{6-\delta}$, Fe leads Cobalt to enter a lesser oxidation state that allows for charge compensation. In reaction circumstances, it prevents Cobalt and the layer doubled perovskites from melting, enabling active surface Co oxy-hydroxide layer to form [128].

Guo et al. [130] show that employing $LaCo_yGa_{1-y}O_3$ mixed oxides as catalysts, alcohols (mostly methanol/ethanol) may be synthesized from syngas. The precursor of segregated cobalt nanoparticles in the LaGaO composite oxide is $La_{1-x}K_xCo_{0.65}Ga_{0.35}O_3$, which boosts its stability in a reactive environment. The impact of K on boosting the dispersion (atomic) of Cobalt and improving the coking composites resistance catalysts is identified by synthesizing La_2O_3 [128].

Steiger et al. [131] examine sulfur tolerance in solid oxide fuel cells and employ segregation reversible Ni to be an element active for the aqueous gas shift process and the second metal transition. Compared to Mn, Mo, Cr, and Fe, only Fe enhances the sulfur tolerance of $La_{0.3}Sr_{0.55}Ti_{0.95}Ni_{0.05}O_3$. Segregation simultaneously of iron and nickel in higher temperatures has little effect on the to and fro segregation reintegration of a couple of metals inside the mixed oxide of perovskite during oxidations, enabling greater time high-temperature uses [128].

Wark and colleagues [132] explain how $LaFeO_3$ works as a photocatalyst in the breakdown of Rhodamine-B and look at the best circumstances for getting the best results. Photoelectrochemical analysis was employed in addition to textural evaluation to explain variations in behavior as a function of calcination temperature. The results indicated lower temperatures boosted separation efficiency with photo-induced charge carrier transfer [128].

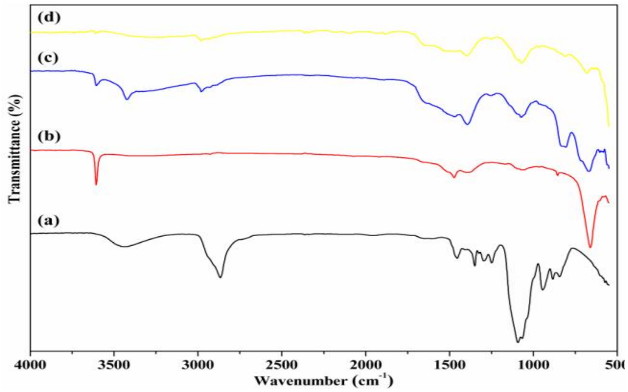

Fig 19: FTIR spectrum of **(a)** ‘PEG 400’, **(b)** ‘product before it is calcined’, **(c)** ‘P700’, and **(d)** ‘P900’. Reproduced with permission from ref. [117]. Copyright 2020 Nano Express

With DFT research by Glisenti et al. [133], replacing La with Sr at the A-site of $LaCoO_3$ decreases the energy required to create oxygen vacancies, which is helpful in three-way catalysts for CO oxidation. Similar results can be produced by switching Co for Cu at the B-site. Effects of substitution appear as higher in $SrTiO_3$ [128].

The impact of some Ti substituting $BaTiO_3$ utilized as lean NOx catalyst trap on NOx storage capacity is investigated by Aldridge et al. [134] Cu is beneficial because it helps to separate Ba_2TiO_4 storage from NOx storage. Among highly active noble metal-based catalysts, $BaTi_{0.8}Cu_{0.2}O_3$ has the most oxygen vacancies and the maximum storage capacity [128].

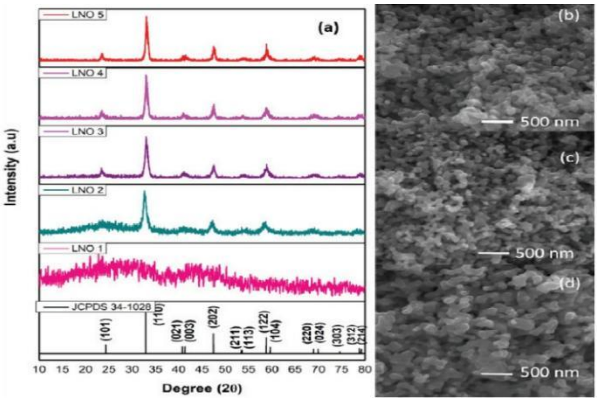

Fig. 20(a) ‘XRD spectrum images of LNO1, LNO2, LNO3, LNO4, and LNO5’ **(b)** ‘Images showing SEM analysis of LNO3’, **(c)** ‘LNO4’ and **(d)** ‘LNO5’ respectively. Reproduced with permission from ref. 120. Copyright 2019 In AIP conference proceedings

Roning and colleagues looked at various $LaCo_{1-x}Mn_xO_3$ and $LaCo_{1-y}Ni_yO_3$ catalysts for NO oxidation to NO_2. [138] While $LaCoO_3$ has the maximum activity among un-doped perovskites, $LaCo_{0.75}Ni_{0.25}O_3$ and $LaCo_{0.75}Ni_{0.25}O_3$ have the highest activity in substituted catalysts, suggesting that perovskites could be used as NO oxidation catalysts in the industry [128].

Heidinger et al. [136] used 3 stages of crushing: a reactive approach that includes high-energy wet ball milling, solid-state synthesis, and low-energy wet ball milling, all of which were subsequently calcined at 400°C. The catalytic efficiency for toluene oxidation improves in both cases after each synthesis phase, per the gain in surface-specific area, which marks about nineteen m^2g^{-1} to $LaFeO_3$ [128].

9. Conclusions and Future Perspective

This review has covered how to manufacture various morphologies of perovskite materials, define perovskite oxides, and employ perovskite oxides in catalysis. Because the sum of oxide needs a higher temperature and a large period of calcination, perovskite oxides are composed of some simple oxides and have a very small surface area. The area and properties of the surface of perovskite oxides must be increased to be used in heterogeneous catalysis or surface reactions. This study demonstrates how to make perovskite oxides in a variety of bulk, nanoscaled, supported, porous, and hollow morphologies, to maximize surface area and surface properties while adhering to reaction conditions. Several methods have been developed to understand perovskite oxides better to analyze their structure and physicochemical characteristics. Perovskite oxides' catalytic properties have been examined regarding their usage in catalysis.

We've already discussed nanoporous perovskite oxides, which can be made using soft and hard templates and colloidal crystal templates. Similarly, template-free and template-assisted synthesis of 1D perovskite oxide nanostructures, as well as thin sheets or multilayers of perovskite oxide and PLD of 2D perovskite oxide nanostructures, have been reported. Chemical solution deposition, CVD and MOCVD, & MBE are also included in PLD (MBE). Top-down and bottom-up methods can be used to make planar perovskite oxide nanostructures in two dimensions. The synthesis of a 3D perovskite oxide nanostructure is also briefly explored.

In characterization, we have reported the characterization of various perovskite oxides namely $SrPdO_3$ by XRD, SEM, TEM, FTIR, XPS, and [(Ba, Sr) TiO_3] by XRD, SEM, TEM, and $Ba_xMn_{1-x}O_3$ by XRD, SEM, EDX and $NdNiO_3$ by XRD, FTIR and $LaNiO_3$ by XRD, SEM respectively.

We compared the catalytic activity of $GdAlO_3$, $SrMnO_3$, $SrCoO_3$, and $MnFeO_3$ to overview the catalytic uses of perovskite oxides. $SrMnO_3$at low temperatures that appearing as a catalyst that is active in most of the four perovskites, according to the findings. Only in the conversion of acetone did $MnFeO_3$ and $SrCoO_{3-x}$ catalysts exhibit strong catalytic activity. We have also reported ABO_3 perovskite in oxidative coupling of methane, $BaCe_{1-x}Mn_xO_{3-\delta}$ perovskite for methane combustion, $Co_xFe_{1-x}O_y$ catalyst for carbon dioxide hydrogenation, $La_{1-x}Sr_xCuO$ catalyst for carbon dioxide hydrogenation to methanol, and metal catalysis on perovskite oxides from recent studies.

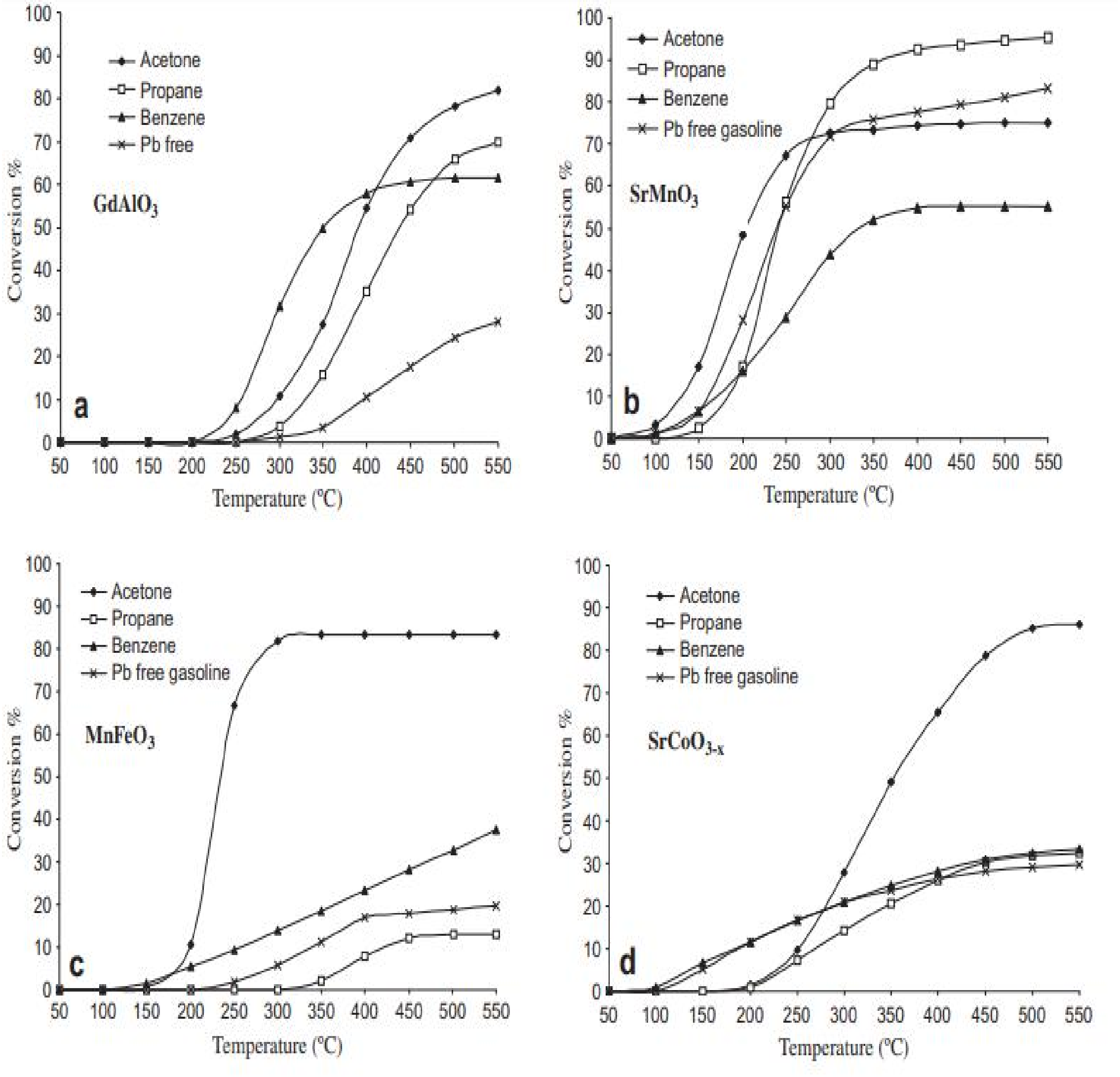

Fig 21: Temperature vs. benzene, propane, acetone, and gasoline of Pb-free conversion by catalytic flameless combustion **(a)** "$GdAlO_3$"**,** **(b)** "$SrMnO_3$", **(c)** "$MnFeO_3$" and **(d)** "$SrCoO_{3-x}$" perovskites. Reproduced with permission from ref. [121]. Copyright 2014 Composites Part B: Engineering

Table 2. T_{10} T_{50} and Kinetic parameters (reaction and rate[a] and activation energy[b]) for perovskite catalysts: Reproduced with permission from ref. [121]

VOCs	GdAlO$_3$				SrMnO$_3$			
	T_{10} (^{O}C)	T_{50} (^{O}C)	Reaction Rate (µmol s^{-1} m^{-2})	Activation energy (KJ / mol)	T_{10} (^{O}C)	T_{50} (^{O}C)	Reaction Rate (µmol s^{-1} m^{-2})	Activation energy (KJ / mol)
Acetone	295	390	6.7 x 10^{-2}	89	130	200	140 x 10^{-2}	37
Propane	330	440	7.8 x 10^{-2}	71	180	240	9.8 x 10^{-2}	31
Benzene	260	350	6.5 x 10^{-2}	68	175	325	26 x 10^{-2}	35
Pb free gasoline	390	-	4.2 x 10^{-1}	62	160	240	55 x 10^{-2}	36

	MnFeO$_3$				SrCoO$_3$			
	T_{10} (^{O}C)	T_{50} (^{O}C)	Reaction Rate (µmol s^{-1} m^{-2})	Activation energy (kJ/ mol)	T_{10} (^{O}C)	T_{50} (^{O}C)	Reaction Rate (µmol s^{-1} m^{-2})	Activation energy (KJ /mol)
Acetone	200	230	65 x 10^{-2}	98	250	325	16 x 10^{-2}	41
Propane	400	-	6.1 x 10^{-2}	80	270	-	3.8 x 10^{-2}	48
Benzene	255	-	17 x 10^{-2}	45	190	-	56 x 10^{-2}	44
Pb free gasoline	340	-	12 x 10^{-2}	47	190	-	11 x 10^{-2}	40

Despite major academic advances over the years, perovskite oxides have failed to find commercial applications as a catalyst. Their limited catalytic efficacy and sensitivity to pollutants like sulfur dioxide could be part of the problem. To commercialize these materials for industrial use, researchers should continue to work on developing a more efficient catalyst and learn more about how toxins interact with the surface of perovskite oxides.

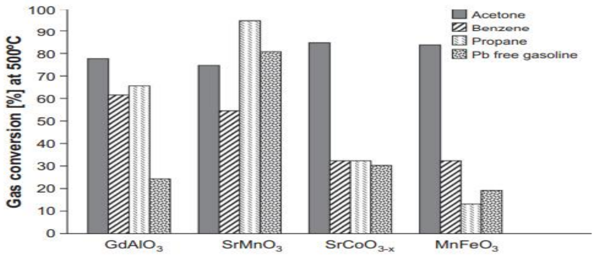

Fig 22: The effect of perovskite catalyst chemical composition on gas conversion at 500°C. Reproduced with permission from ref. [121]. Copyright 2014 Composites Part B: Engineering

Acknowledgment

This work is financially supported by Chemistry Department, University of Wah.

Conflict of interest

The authors reported no potential conflict of interest.

Authors Contribution

F. A and S.Y.B convinced the main idea and wrote the manuscript. K.e.K, S.F revised the manuscript and prepared figures and references.

References

1. Zhu, J., et al., Perovskite oxides: preparation, characterizations, and applications in heterogeneous catalysis. ACS Catalysis, 2014. 4(9): p. 2917-2940. DOI: https://doi.org/10.1021/cs500606g.
2. Rojas, M., et al., Preparation and characterization of LaMn1− xCuxO$_3$+ λ perovskite oxides. Journal of Catalysis, 1990. 124(1): p. 41-51. DOI: https://doi.org/10.1016/0021-9517(90)90102-P.
3. Labhasetwar, N., et al., Perovskite-type catalytic materials for environmental applications. Science and technology of advanced materials, 2015. DOI: https://doi.org/10.1088/1468-6996/16/3/036002.
4. Sun, C., J.A. Alonso, and J. Bian, Recent advances in perovskite-type oxides for energy conversion and storage applications. Advanced Energy Materials, 2021. 11(2): p. 2000459. DOI: https://doi.org/10.1002/aenm.202000459.
5. Pena, M. and J. Fierro, Chemical structures and

performance of perovskite oxides. Chemical reviews, 2001. 101(7): p. 1981-2018.

DOI: https://doi.org/10.1021/cr980129f.

6. Nagai, T., et al., Synthesis of nano-sized perovskite-type oxide with the use of polyvinyl pyrrolidone. Journal of Asian Ceramic Societies, 2014. 2(4): p. 329-332.

   DOI: https://doi.org/10.1016/j.jascer.2014.08.004.

7. Siemons, M., et al., Preparation of Nanosized Perovskite-type Oxides via Polyol Method. Zeitschrift für anorganische und allgemeine Chemie, 2004. 630(12): p. 2083-2089.

   DOI: https://doi.org/10.1002/zaac.200400300.

8. Shao, Z., W. Zhou, and Z. Zhu, Advanced synthesis of materials for intermediate-temperature solid oxide fuel cells. Progress in Materials Science, 2012. 57(4): p. 804-874.

   DOI: https://doi.org/10.1016/j.pmatsci.2011.08.002.

9. Shen, Z., et al., $BaTiO_3$–$BiYbO_3$ perovskite materials for energy storage applications. Journal of Materials Chemistry A, 2015. 3(35): p. 18146-18153.

   DOI: https://doi.org/10.1039/C5TA03614C

10. Zhu, Y., et al., Phosphorus-doped perovskite oxide as highly efficient water oxidation electrocatalyst in alkaline solution. Advanced Functional Materials, 2016. 26(32): p. 5862-5872.

    DOI: https://doi.org/10.1002/adfm.201601902.

11. Zhang, Z., et al., Tin-doped perovskite mixed conducting membrane for efficient air separation. Journal of Materials Chemistry A, 2014. 2(25): p. 9666-9674.

    DOI: https://doi.org/10.1039/C4TA00926F

12. Pramana, S.S., et al., Crystal structure and surface characteristics of Sr-doped $GdBaCo_2O_{6-\delta}$ double perovskites: oxygen evolution reaction and conductivity. Journal of Materials Chemistry A, 2018. 6(13): p. 5335-5345.

    DOI: 10.1039/C7TA06817D.

13. Chen, Y., et al., Exceptionally active iridium evolved from a pseudo-cubic perovskite for oxygen evolution in acid. Nature communications, 2019. 10(1): p. 1-10.

    DOI: https://doi.org/10.1038/s41467-019-08532-3

14. Yu, J., et al., Advances in porous perovskites: synthesis and electrocatalytic performance in fuel cells and metal–air batteries. Energy & Environmental Materials, 2020. 3(2): p. 121-145.

    DOI: https://doi.org/10.1002/eem2.12064.

15. Zhu, Y., et al., SrNb0. 1Co0. 7Fe0. 2O3− δ perovskite as a next-generation electrocatalyst for oxygen evolution in alkaline solution. Angewandte Chemie, 2015. 127(13): p. 3969-3973.

    DOI: https://doi.org/10.1002/ange.201408998.

16. Bai, S., et al., High-power Li-metal anode enabled by metal-organic framework modified electrolyte. Joule, 2018. 2(10): p. 2117-2132.

    DOI: https://doi.org/10.1016/j.joule.2018.07.010.

17. Liu, H., et al., Cation deficiency design: A simple and efficient strategy for promoting oxygen evolution reaction activity of perovskite electrocatalyst. Electrochimica Acta, 2018. 259: p. 1004-1010.

    DOI: https://doi.org/10.1016/j.electacta.2017.10.172.

18. Tien-Thao, N., et al., Effect of alkali additives over nanocrystalline Co–Cu-based perovskites as catalysts for higher-alcohol synthesis. Journal of Catalysis, 2007. 245(2): p. 348-357.

    DOI: https://doi.org/10.1016/j.jcat.2006.10.026.

19. Li, R., et al., Realizing fourfold enhancement in conductivity of perovskite Li0. 33La0. 557TiO3 electrolyte membrane via a Sr and Ta co-doping strategy. Journal of Membrane Science, 2019. 582: p. 194-202.

    DOI: https://doi.org/10.1016/j.memsci.2019.03.074.

20. Yu, R., et al., Synthesis and characterization of perovskite-type (Li, Sr)(Zr, Nb) O3 quaternary solid electrolyte for all-solid-state batteries. Journal of Power Sources, 2016. 306: p. 623-629. DOI: https://doi.org/10.1016/j.jpowsour.2015.12.065.

21. Song, S., et al., Molten-salt synthesis of porous LaO. 6SrO. 4CoO. 2FeO.8O_2. perovskite as an efficient electrocatalyst for oxygen evolution. Nano Res., 2018. 11(9): p. 4796-4805.

    DOI: https://doi.org/10.1007/s12274-018-2065-1

22. Mendoza-Mendoza, E., et al., Molten salts synthesis and electrical properties of Sr-and/or Mg-doped perovskite-type $LaAlO_3$ powders. Journal of Materials Science, 2012. 47(16): p. 6076-6085.

    DOI: https://doi.org/10.1007/s10853-012-6520-1

23. Huang, X., et al., Facile synthesis of porous spherical $La_{0.8}Sr_{0.2}Mn_{1-x}Cu_xO_3$ ($0\leq x\leq 0.4$) and nanocubic $La_{0.8}Sr_{0.2}MnO_3$ with high catalytic activity for CO. CrystEngComm, 2018. 20(43): p. 7020-7029.

    DOI: https://doi.org/10.1039/C8CE01000E.

24. Wang, Y., et al., Morphologically controlled synthesis of porous spherical and cubic LaMnO3 with high activity for the catalytic removal of toluene. ACS applied materials &

interfaces, 2014. 6(20): p. 17394-17401.

DOI: https://doi.org/10.1021/am500489x.

25. Song, Z., et al., Recent progress on MOF-derived nanomaterials as advanced electrocatalysts in fuel cells. Catalysts, 2016. 6(8): p. 116.

DOI: https://doi.org/10.3390/catal6080116.

26. Shin, J.F., et al., Self-assembled dynamic perovskite composite cathodes for intermediate temperature solid oxide fuel cells. Nature Energy, 2017. 2(3): p. 1-7.

DOI: https://doi.org/10.1038/nenergy.2016.214

27. Sun, H., et al., Multi-active sites derived from a single/double perovskite hybrid for highly efficient water oxidation. Electrochimica Acta, 2019. 299: p. 926-932.

DOI: https://doi.org/10.1016/j.electacta.2019.01.067.

28. Yang, G., et al., Enhancing electrode performance by exsolved nanoparticles: a superior cobalt-free perovskite electrocatalyst for solid oxide fuel cells. ACS applied materials & interfaces, 2016. 8(51): p. 35308-35314.

DOI: https://doi.org/10.1021/acsami.6b12157

29. Zahrani, E.M. and M. Fathi, The effect of high-energy ball milling parameters on the preparation and characterization of fluorapatite nanocrystalline powder. Ceramics International, 2009. 35(6): p. 2311-2323.

DOI: https://doi.org/10.1016/j.ceramint.2009.01.012.

30. Zhang, R., H. Alamdari, and S. Kaliaguine, SO2 poisoning of LaFe0. 8Cu0. 2O3 perovskite prepared by reactive grinding during NO reduction by C3H6. Applied Catalysis A: General, 2008. 340(1): p. 140-151.

DOI: https://doi.org/10.1016/j.apcata.2008.02.028.

31. Tien-Thao, N., et al., LaCo1− xCuxO3− δ perovskite catalysts for higher alcohol synthesis. Applied Catalysis A: General, 2006. 311: p. 204-212.

DOI: https://doi.org/10.1016/j.apcata.2006.06.029.

32. Li, L., et al., Topochemical molten salt synthesis for functional perovskite compounds. Chemical science, 2016. 7(2): p. 855-865.

DOI: 10.1039/C5SC03521J.

33. Song, Y.-L., et al., Molten salt synthesis and supercapacitor properties of oxygen-vacancy LaMnO3−δ. Journal of Energy Chemistry, 2020. 43: p. 173-181.

DOI: https://doi.org/10.1016/j.jechem.2019.09.007.

34. Liu, X., et al., Enhanced microwave absorption properties by tuning cation deficiency of perovskite oxides of two-dimensional LaFeO3/C composite in X-band. ACS applied materials & interfaces, 2017. 9(8): p. 7601-7610.

DOI: https://doi.org/10.1021/acsami.6b15379

35. Fechler, N., T.P. Fellinger, and M. Antonietti, “Salt templating”: a simple and sustainable pathway toward highly porous functional carbons from ionic liquids. Advanced Materials, 2013. 25(1): p. 75-79.

DOI: https://doi.org/10.1002/adma.201203422.

36. Liu, X. and M. Antonietti, Moderating black powder chemistry for the synthesis of doped and highly porous graphene nanoplatelets and their use in electrocatalysis. Advanced Materials, 2013. 25(43): p. 6284-6290.

DOI: https://doi.org/10.1002/adma.201302034.

37. Mao, Y., S. Banerjee, and S.S. Wong, Large-scale synthesis of single-crystalline perovskite nanostructures. Journal of the American Chemical Society, 2003. 125(51): p. 15718-15719.

DOI: https://doi.org/10.1021/ja038192w

38. Kačenka, M., et al., The magnetic and neutron diffraction studies of La1− xSrxMnO3 nanoparticles prepared via molten salt synthesis. Journal of Solid State Chemistry, 2015. 221: p. 364-372.

DOI: https://doi.org/10.1016/j.jssc.2014.10.024.

39. Li, F., et al., Solid-State Synthesis of LaCoO3 Perovskite Nanocrystals. Journal of the American Ceramic Society, 2002. 85(9): p. 2177-2180.

DOI: https://doi.org/10.1111/j.1151-2916.2002.tb00431.x.

40. Deng, X., et al., Molten salt synthesis of nitrogen-doped carbon with hierarchical pore structures for use as high-performance electrodes in supercapacitors. Carbon, 2015. 93: p. 48-58.

DOI: https://doi.org/10.1016/j.carbon.2015.05.031.

41. Zhou, H., Y. Mao, and S.S. Wong, Probing structure− parameter correlations in the molten salt synthesis of BaZrO3 perovskite submicrometer-sized particles. Chemistry of Materials, 2007. 19(22): p. 5238-5249.

DOI: https://doi.org/10.1021/cm071456j.

42. Sun, Y.-F., et al., Smart tuning of 3D ordered electrocatalysts for enhanced oxygen reduction reaction. Applied Catalysis B: Environmental, 2017. 219: p. 640-644.

DOI: https://doi.org/10.1016/j.apcatb.2017.08.017.

43. Yang, Y., et al., In Situ Tetraethoxysilane-Templated Porous BaO. 5SrO. 5CoO. 8Fe0. 2$O_{3-\delta}$ Perovskite for the Oxygen Evolution Reaction. ChemElectroChem, 2015. 2(2): p. 200-203.

DOI: https://doi.org/10.1002/celc.201402279.

44. Xu, Y., et al., Carbon-coated perovskite BaMnO3 porous nanorods with enhanced electrocatalytic perporites for oxygen reduction and oxygen evolution. Electrochimica Acta, 2015. 174: p. 551-556.

DOI: https://doi.org/10.1016/j.electacta.2015.05.184.

45. Sennu, P., et al., Exceptional catalytic activity of hollow structured $La_{0.6}Sr_{0.4}CoO_{3-\delta}$ perovskite spheres in aqueous media and aprotic LiO_2 batteries. Journal of Materials Chemistry A, 2017. 5(34): p. 18029-18037.

DOI: https://doi.org/10.1039/C7TA04189F.

46. Han, X., et al., Porous perovskite $CaMnO_3$ as an electrocatalyst for rechargeable LiO_2 batteries. Chemical Communications, 2014. 50(12): p. 1497-1499.

DOI: https://doi.org/10.1039/C3CC48207C

47. Bu, Y., et al., A highly efficient and robust cation ordered perovskite oxide as a bifunctional catalyst for rechargeable zinc-air batteries. Acs Nano, 2017. 11(11): p. 11594-11601.

DOI: https://doi.org/10.1021/acsnano.7b06595.

48. Ashok, A., et al., Combustion synthesis of bifunctional LaMO3 (M= Cr, Mn, Fe, Co, Ni) perovskites for oxygen reduction and oxygen evolution reaction in alkaline media. Journal of Electroanalytical Chemistry, 2018. 809: p. 22-30.

DOI: https://doi.org/10.1016/j.jelechem.2017.12.043.

49. Zhu, Y., et al., A perovskite nanorod as bifunctional electrocatalyst for overall water splitting. Advanced Energy Materials, 2017. 7(8): p. 1602122.

DOI: https://doi.org/10.1002/aenm.201602122

50. Zhao, Y., et al., Hierarchical mesoporous perovskite $La_{0.5}Sr_{0.5}CoO_2$. nanowires with ultrahigh capacity for Li-air batteries. Proceedings of the National Academy of Sciences, 2012. 109(48): p. 19569-19574.

DOI: https://doi.org/10.1073/pnas.121031510.

51. Liu, L., et al., In situ fabrication of highly active γ-MnO_2/$SmMnO_3$ catalyst for deep catalytic oxidation of gaseous benzene, ethylbenzene, toluene, and o-xylene. Journal of hazardous materials, 2019. 362: p. 178-186.

DOI: https://doi.org/10.1016/j.jhazmat.2018.09.012.

52. Jiang, S., et al., Hierarchical porous cobalt-free perovskite electrode for highly efficient oxygen reduction. Journal of Materials Chemistry, 2012. 22(32): p. 16214-16218.

DOI: https://doi.org/10.1039/C2JM33311B.

53. He, J., et al., 3D ordered macroporous SmCoO3 perovskite for highly active and selective hydrogen peroxide detection. Electrochimica Acta, 2018. 260: p. 372-383.

DOI: https://doi.org/10.1016/j.electacta.2017.12.084.

54. Zhuang, S., et al., Preparation of homogeneous nanoporous LaO. 6CaO. 4CoO_3 for bi-functional catalysis in an alkaline electrolyte. Electrochemistry communications, 2011. 13(4): p. 321-324. DOI: https://doi.org/10.1016/j.elecom.2011.01.014.

55. Zhen, D., et al., Electrospun porous perovskite La0.6Sr0. 4Co1–xFexO3–δ nanofibers for efficient oxygen evolution reaction. Advanced Materials Interfaces, 2017. 4(13): p. 1700146.

DOI: https://doi.org/10.1002/admi.201700146

56. Jin, C., et al., Electrochemical study of Ba0. 5Sr0. 5Co0. 8Fe0. 2O3 perovskite as bifunctional catalyst in alkaline media. international journal of hydrogen energy, 2013. 38(25): p. 10389-10393.

DOI: https://doi.org/10.1016/j.ijhydene.2013.06.047.

57. Gosavi, P.V. and R.B. Biniwale, Pure phase $LaFeO_3$ perovskite with improved surface area synthesized using different routes and its characterization. Materials Chemistry and Physics, 2010. 119(1-2): p. 324-329.

DOI: https://doi.org/10.1016/j.matchemphys.2009.09.005.

58. Pham, T.V., et al., Carbon-and binder-free 3D porous perovskite oxide air electrode for rechargeable lithium–oxygen batteries. Journal of Materials Chemistry A, 2017. 5(11): p. 5283-5289. DOI: https://doi.org/10.1039/C6TA10751F.

59. Hua, B., et al., All-in-one perovskite catalyst: smart controls of architecture and composition toward enhanced oxygen/hydrogen evolution reactions. Advanced Energy Materials, 2017. 7(20): p. 1700666.

DOI: https://doi.org/10.1002/aenm.201700666

60. Pinna, N. and M. Niederberger, Surfactant-free nonaqueous synthesis of metal oxide nanostructures. Angewandte Chemie International Edition, 2008. 47(29): p. 5292-5304.

DOI: https://doi.org/10.1002/anie.200704541

61. Fu, S., et al., Low temperature synthesis and photocatalytic property of perovskite-type $LaCoO_3$ hollow spheres. Journal of Alloys and Compounds, 2013. 576: p. 5-12.

DOI: https://doi.org/10.1016/j.jallcom.2013.04.092.

62. Ji, K., et al., One-pot hydrothermal preparation and catalytic performance of porous strontium ferrite hollow spheres for the combustion of toluene. Journal of Molecular Catalysis A: Chemical, 2013. 370: p. 189-196.DOI: https://doi.org/10.1016/j.molcata.2013.01.013.

63. Gao, P., et al., Perovskite LaMnO3 hollow nanospheres: The synthesis and the application in catalytic wet air oxidation of phenol. Materials Letters, 2013. 92: p. 173-176.

    DOI: https://doi.org/10.1016/j.matlet.2012.10.091.

64. Kim, Y., et al., Ferromagnetic nanospheres of perovskite manganite $La_{0.7}Ca_{0.3}MnO_3$ prepared by template replication in porous carbon framework. Journal of applied physics, 2004. 95(11): p. 7088-7090.

    DOI: https://doi.org/10.1063/1.1687634.

65. Ko, Y., C.L. Cahill, and J. Parise, Novel layered sulfides of tin: synthesis and structural characterization of $Cs_4Sn_5S_{12}·2H_2O$ and Sn_5S_{12} ($N_2C_4H_{11}$) 2 ($N_4C_{10}H_{24}$). Journal of the Chemical Society, Chemical Communications, 1994(1): p. 69-70

    DOI: https://doi.org/10.1039/C39940000069

66. Kresge, a.C., et al., Ordered mesoporous molecular sieves synthesized by a liquid-crystal template. mechanism. nature, 1992. 359(6397): p. 710-712.

    DOI: https://doi.org/10.1038/359710a0

67. Zhao, D., et al., Triblock copolymer syntheses of mesoporous silica with periodic 50 to 300 angstrom pores. science, 1998. 279(5350): p. 548-552.

    DOI: 10.1126/science.279.5350.548.

68. Grosso, C., B.S. Boissiere, and N.P. T Brezesinski, P. Albouy, H. Amenitsch, M. Antonietti, and C. Sanchez,"Periodically Ordered Nanoscale Islands and Mesoporous Films Composed of Nanocrystalline Multimetallic Oxides,". Nat. Mater, 2004. 3(11): p. 787-92.

    DOI: https://doi.org/10.1038/nmat1206

69. Reitz, C., et al., Nanocrystalline NaTaO 3 thin film materials with ordered 3D mesoporous and nanopillar-like structures through PIB-b-PEO polymer templating: Towards high-performance UV-light photocatalysts. RSC advances, 2012. 2(12): p. 5130-5133.

    DOI: 10.1039/C2RA20203D.

70. Lertpanyapornchai, B., T. Yokoi, and C. Ngamcharussrivichai, Citric acid as complexing agent in synthesis of mesoporous strontium titanate via neutral-templated self-assembly sol–gel combustion method. Microporous and Mesoporous Materials, 2016. 226: p. 505-509.

    DOI: https://doi.org/10.1016/j.micromeso.2016.02.020.

71. Suzuki, N., et al., Synthesis of highly strained mesostructured $SrTiO_3/BaTiO_3$ composite films with robust ferroelectricity. Chemistry–A European Journal, 2013. 19(14): p. 4446-4450.

    DOI: https://doi.org/10.1002/chem.201203421.

72. Hou, R., P. Ferreira, and P. Vilarinho, A facile route for synthesis of mesoporous barium titanate crystallites. Microporous and mesoporous materials, 2008. 110(2-3): p. 392-396.

    DOI: https://doi.org/10.1016/j.micromeso.2007.06.051.

73. Huang, X., et al., Synthesis and applications of nanoporous perovskite metal oxides. Chemical science, 2018. 9(15): p. 3623-3637.

    DOI: 10.1039/C7SC03920D.

74. Gu, D. and F. Schüth, Synthesis of non-siliceous mesoporous oxides. Chemical Society Reviews, 2014. 43(1): p. 313-344.

    DOI: 10.1039/C3CS60155B.

75. Ren, Y., Z. Ma, and P.G. Bruce, Ordered mesoporous metal oxides: synthesis and applications. Chemical Society Reviews, 2012. 41(14): p. 4909-4927.

    DOI: https://doi.org/10.1039/C2CS35086F

76. Wang, Y., et al., Nanocasted synthesis of mesoporous $LaCoO_3$ perovskite with extremely high surface area and excellent activity in methane combustion. The Journal of Physical Chemistry C, 2008. 112(39): p. 15293-15298.

    DOI: https://doi.org/10.1021/jp8048394.

77. Nair, M.M., F. Kleitz, and S. Kaliaguine, Kinetics of methanol oxidation over mesoporous perovskite catalysts. ChemCatChem, 2012. 4(3): p. 387-394.

    DOI: https://doi.org/10.1002/cctc.201100356.

78. De Lima, R., et al., High specific surface area LaFeCo perovskites—Synthesis by nanocasting and catalytic behavior in the reduction of NO with CO. Applied Catalysis B: Environmental, 2009. 90(3-4): p. 441-450.

    DOI: https://doi.org/10.1016/j.apcatb.2009.04.004.

79. Huang, X., et al., Effect of metal species on the morphology of metal (oxides) within mesochannels of SBA-15 via a double-solvent method. Microporous and Mesoporous Materials, 2015. 207: p. 105-110.

    DOI: https://doi.org/10.1016/j.micromeso.2015.01.008.

80. Huang, X., et al., Effect of surface properties of SBA-15 on confined Ag nanomaterials via double solvent technique. Microporous and mesoporous materials, 2011. 144(1-3): p. 171-175.

    DOI: https://doi.org/10.1016/j.micromeso.2011.04.012.

81. Stein, A., F. Li, and N.R. Denny, Morphological control in colloidal crystal templating of inverse opals, hierarchical structures, and shaped particles. Chemistry of

Materials, 2008. 20(3): p. 649-666.

DOI: https://doi.org/10.1021/cm702107n.

82. Chi, E.O., et al., A macroporous perovskite manganite from colloidal templates with a Curie temperaure of 320 K. Chemistry of materials, 2003. 15(10): p. 1929-1931.

DOI: https://doi.org/10.1021/cm034031f.

83. Xu, J., et al., Three-dimensionally ordered macroporous $LaCoxFe_{1-x}O_3$ perovskite-type complex oxide catalysts for diesel soot combustion. Catalysis Today, 2010. 153(3-4): p. 136-142.

DOI: https://doi.org/10.1016/j.cattod.2010.01.063.

84. Zhao, Z., et al., Three-dimensionally ordered macroporous La0. 6Sr0. 4FeO3− δ: High-efficiency catalysts for the oxidative removal of toluene. Microporous and mesoporous materials, 2012. 163: p. 131-139.

DOI: https://doi.org/10.1016/j.micromeso.2012.07.006.

85. Arandiyan, H., et al., Three-dimensionally ordered macroporous La0. 6Sr0. 4MnO3 with high surface areas: active catalysts for the combustion of methane. Journal of Catalysis, 2013. 307: p. 327-339.

DOI: https://doi.org/10.1016/j.jcat.2013.07.013.

86. Arandiyan, H., et al., Three-dimensionally ordered macroporous $La_{0.6}Sr_{0.4}MnO_3$ supported Ag nanoparticles for the combustion of methane. The Journal of Physical Chemistry C, 2014. 118(27): p. 14913-14928.

DOI: https://doi.org/10.1021/jp502256t.

87. Guo, G., et al., Three dimensionally ordered macroporous Pd–LaMnO 3 self-regeneration catalysts for methane combustion. Chemical Communications, 2014. 50(88): p. 13575-13577.

DOI: https://doi.org/10.1039/C4CC05966B.

88. Joshi, U.A., et al., Surfactant-free hydrothermal synthesis of highly tetragonal barium titanate nanowires: a structural investigation. The Journal of Physical Chemistry B, 2006. 110(25): p. 12249-12256.

DOI: https://doi.org/10.1021/jp0600110.

89. Wang, J., et al., Mechanism of hydrothermal growth of ferroelectric PZT nanowires. Journal of crystal growth, 2012. 347(1): p. 1-6.

DOI: https://doi.org/10.1016/j.jcrysgro.2012.03.022.

90. Chen, X., et al., 1.6 V nanogenerator for mechanical energy harvesting using PZT nanofibers. Nano letters, 2010. 10(6): p. 2133-2137.

DOI: https://doi.org/10.1021/nl100812k.

91. Rao, S., et al., Weakening of charge order and antiferromagnetic to ferromagnetic switch over in Pr 0.5 Ca 0.5 MnO 3 nanowires. Applied Physics Letters, 2005. 87(18): p. 182503.

DOI: https://doi.org/10.1063/1.2125129.

92. McQuaid, R., et al., Domain wall propagation in meso- and nanoscale ferroelectrics. Journal of Physics: Condensed Matter, 2011. 24(2): p. 024204.

DOI: https://doi.org/10.1088/0953-8984/24/2/024204.

93. Mao, Y., S. Banerjee, and S.S. Wong, Hydrothermal synthesis of perovskite nanotubes. Chemical communications, 2003(3): p. 408-409.

DOI: https://doi.org/10.1039/B210633G.

94. Fu, L., et al., Magnetic, electronic, and optical properties of perovskite materials, in Revolution of Perovskite. 2020, Springer. p. 43-59.

DOI: 10.1039/D1RA08185C.

95. Xia, W., Y. Lu, and X. Zhu, Preparation Methods of Perovskite-Type Oxide Materials, in Revolution of Perovskite. 2020, Springer. p. 61-93.

DOI: https://doi.org/10.1007/978-981-15-1267-4_3

96. Shankar, K.S. and A. Raychaudhuri, Growth of an ordered array of oriented manganite nanowires in alumina templates. Nanotechnology, 2004. 15(9): p. 1312.

DOI: https://doi.org/10.1088/0957-4484/15/9/034.

97. Chen, F., et al., Synthesis and characterization of La0. 825Sr0.175MnO3 nanowires. Journal of Physics: Condensed Matter, 2005. 17(44): p. L467.

DOI: https://doi.org/10.1088/0953-8984/17/44/L02.

98. Hernandez, B.A., et al., Sol− gel template synthesis and characterization of BaTiO3 and PbTiO3 nanotubes. Chemistry of Materials, 2002. 14(2): p. 480-482.

DOI: https://doi.org/10.1021/cm010998c.

99. Sousa, C., et al., Rapid synthesis of ordered manganite nanotubes by microwave irradiation in alumina templates. Journal of nanoscience and nanotechnology, 2009. 9(10): p. 6084-6088.

DOI: https://doi.org/10.1166/jnn.2009.1572

100. Tagliazucchi, M., et al., Synthesis of lanthanum nickelate perovskite nanotubes by using a template-inorganic precursor. Solid state communications, 2006. 137(4): p. 212-215.

DOI: https://doi.org/10.1016/j.ssc.2005.11.022.

101. Bassiri-Gharb, N., Y. Bastani, and A. Bernal, Chemical solution growth of ferroelectric oxide thin films and nanostructures. Chemical Society Reviews, 2014. 43(7): p. 2125-2140.

DOI: https://doi.org/10.1039/C3CS60250H.

102. Schwartz, R.W., Chemical solution deposition of perovskite thin films. Chemistry of materials, 1997. 9(11): p. 2325-2340.

DOI: https://doi.org/10.1021/cm970286f.

103. Zhang, Q., D. Sando, and V. Nagarajan, Chemical route derived bismuth ferrite thin films and nanomaterials. Journal of Materials Chemistry C, 2016. 4(19): p. 4092-4124.

DOI: https://doi.org/10.1039/C6TC00243A.

104. Wang, H., G. Meng, and D. Peng, Aerosol and plasma assisted chemical vapor deposition process for multi-component oxide La0. 8Sr0. 2MnO3 thin film. Thin Solid Films, 2000. 368(2): p. 275-278.

DOI: https://doi.org/10.1016/S0040-6090(00)00781-1.

105. Weiss, F., et al., Multifunctional oxide nanostructures by metal-organic chemical vapor deposition (MOCVD). Pure and Applied Chemistry, 2009. 81(8): p. 1523-1534.

DOI: https://doi.org/10.1351/PAC-CON-08-08-10.

106. Ahluwalia, R., et al., Manipulating ferroelectric domains in nanostructures under electron beams. Physical review letters, 2013. 111(16): p. 165702.

DOI: https://doi.org/10.1103/PhysRevLett.111.165702

107. Lee, W., et al., Individually addressable epitaxial ferroelectric nanocapacitor arrays with near Tb inch− 2 density. Nature Nanotechnology, 2008. 3(7): p. 402-407.

DOI: https://doi.org/10.1038/nnano.2008.161

108. Li, Y., et al., Physical processes-aided periodic micro/nanostructured arrays by colloidal template technique: fabrication and applications. Chemical Society Reviews, 2013. 42(8): p. 3614-3627.

DOI: https://doi.org/10.1039/C3CS35482B.

109. Atta, N.F., A. Galal, and E.H. El-Ads, Perovskite nanomaterials–synthesis, characterization, and applications. Perovskite Materials–Synthesis, Characterisation, Properties, and Applications; Pan, L., Ed, 2016: p. 107-151.

DOI: http:/ / dx.doi.org/10.5772/61280

110. Atta, N.F., et al., Nano-perovskite carbon paste composite electrode for the simultaneous determination of dopamine, ascorbic acid and uric acid. Electrochimica Acta, 2014. 128: p. 16-24.

DOI: https://doi.org/10.1016/j.electacta.2013.09.101.

111. Srivastava, A., et al., Effect of cation doping on low-temperature specific heat of LaMnO3 manganite. Journal of Magnetism and Magnetic Materials, 2008. 320(21): p. 2596-2601

DOI: https://doi.org/10.1016/j.jmmm.2008.05.042

112. Maroneze, C.M., et al., Electroactive properties of 1-propyl-3-methylimidazolium ionic liquid covalently bonded on mesoporous silica surface: development of an electrochemical sensor probed for NADH, dopamine and uric acid detection. Electrochimica Acta, 2014. 123: p. 435-440.

DOI: https://doi.org/10.1016/j.electacta.2014.01.071.

113. Vijayakumar, C., et al., Synthesis, characterization, sintering and dielectric properties of nanostructured perovskite-type oxide, Ba2GdSbO6. Bulletin of Materials Science, 2008. 31(5): p. 719-722

DOI: https://doi.org/10.1007/s12034-008-0113-2

114. Cho, Y.-G., et al., Characterization and catalytic properties of surface La-rich LaFeO 3 perovskite. Bulletin of the Korean Chemical Society, 2009. 30(6): p. 1368-1372.

DOI: https://doi.org/10.5012/bkcs.2009.30.6.1368

115. Qi, J.Q., et al., Direct large-scale synthesis of perovskite barium strontium titanate nano-particles from solutions. Journal of Solid State Chemistry, 2005. 178(1): p. 279-284.

DOI: https://doi.org/10.1016/j.jssc.2004.12.003.

116. Rafique, M., et al., Fabrication of novel perovskite oxide BaxMn1− xO3 electrode for supercapacitors. International Journal of Energy Research, 2021. 45(3): p. 4145-4154.

DOI: https://doi.org/10.1002/er.6075.

117. Medina, M., et al., Low oxygen pressure synthesis of NdNiO3-δ nanowires by electrospinning. Nano Express, 2020. 1(1): p. 010028

DOI: https://doi.org/10.1088/2632-959X/ab8a77

118. Qiao, H., et al., Preparation and characterization of NiO nanoparticles by anodic arc plasma method. Journal of Nanomaterials, 2009. 2009.

DOI: https://doi.org/10.1155/2009/795928.

119. Li, R., et al., Large scale synthesis of NiCo layered double hydroxides for superior asymmetric electrochemical capacitor. Scientific reports, 2016. 6(1): p. 1-9.

DOI: https://doi.org/10.1038/srep18737

120. Harikrishnan, M. and A.C. Bose. LaNiO3 perovskite oxides by co-precipitation method as electrode for high performance supercapacitor. in AIP Conference Proceedings. 2019. AIP Publishing LLC.

DOI: https://doi.org/10.1063/1.5112968.

121. Rezlescu, N., et al., Characterization and catalytic properties of some perovskites. Composites Part B:

Engineering, 2014. 60: p. 515-522.
DOI: https://doi.org/10.1016/j.compositesb.2014.01.006.

122. Seyfi, B., M. Baghalha, and H. Kazemian, Modified LaCoO3 nano-perovskite catalysts for the environmental application of automotive CO oxidation. Chemical Engineering Journal, 2009. 148(2-3): p. 306-311.
DOI: https://doi.org/10.1016/j.cej.2008.08.041.

123. Sim, Y., et al., Catalytic behavior of ABO3 perovskites in the oxidative coupling of methane. Molecular Catalysis, 2020. 489: p. 110925.
DOI: https://doi.org/10.1016/j.mcat.2020.110925.

124. Tan, X., et al., Investigation of perovskite BaCe1-xMnxO3-δ for methane combustion. Ceramics International, 2021. 47(7): p. 8762-8768.
DOI: https://doi.org/10.1016/j.ceramint.2020.11.141.

125. Meng, M., et al., Mechanochemical redox synthesis of interstitial mesoporous CoxFe1-xOy catalyst for CO2 hydrogenation. Greenhouse Gases: Science and Technology, 2021.
DOI: https://doi.org/10.1002/ghg.2108.

126. Poerjoto, A.J., et al., The role of lattice oxygen in CO2 hydrogenation to methanol over La1-xSrxCuO catalysts. Journal of CO2 Utilization, 2021. 47: p. 101498.
DOI: https://doi.org/10.1016/j.jcou.2021.101498.

127. Rojas-Cervantes, M.L. and E. Castillejos, Perovskites as catalysts in advanced oxidation processes for wastewater treatment. Catalysts, 2019. 9(3): p. 230.
DOI: https://doi.org/10.3390/catal9030230.

128. Ferri, D., Catalysis by Metals on Perovskite-Type Oxides. 2020, Multidisciplinary Digital Publishing Institute.
DOI: https://doi.org/10.3390/catal10091062.

129. Kim, B.-J., et al., Fe-Doping in Double Perovskite PrBaCo2 (1-x) Fe2xO6-δ: Insights into Structural and Electronic Effects to Enhance Oxygen Evolution Catalyst Stability. Catalysts, 2019. 9(3): p. 263.
DOI: https://doi.org/10.3390/catal9030263.

130. Guo, S., et al., K-Modulated Co nanoparticles trapped in La-Ga-O as superior catalysts for higher alcohols synthesis from syngas. Catalysts, 2019. 9(3): p. 218.
DOI: https://doi.org/10.3390/catal9030218.

131. Steiger, P., et al., Segregation of Nickel/Iron Bimetallic Particles from Lanthanum Doped Strontium Titanates to Improve Sulfur Stability of Solid Oxide Fuel Cell Anodes. Catalysts, 2019. 9(4): p. 332.
DOI: https://doi.org/10.3390/catal9040332.

132. Ismael, M. and M. Wark, Perovskite-type LaFeO3: photoelectrochemical properties and photocatalytic degradation of organic pollutants under visible light irradiation. Catalysts, 2019. 9(4): p. 342.
DOI: https://doi.org/10.3390/catal9040342.

133. Glisenti, A. and A. Vittadini, On the Effects of Doping on the Catalytic Performance of (La, Sr) CoO3. A DFT Study of CO Oxidation. Catalysts, 2019. 9(4): p. 312.
DOI: https://doi.org/10.3390/catal9040312.

134. Aldridge, C., et al., BaTi0. 8B0. 2O3 (B= Mn, Fe, Co, Cu) LNT Catalysts: Effect of Partial Ti Substitution on NOx Storage Capacity. Catalysts, 2019. 9(4): p. 365.
DOI: https://doi.org/10.3390/catal9040365.

135. Hyrve, S.M., et al., Catalytic Oxidation of NO over LaCo1− xBxO3 (B= Mn, Ni) Perovskites for Nitric Acid Production. Catalysts, 2019. 9(5): p. 429.
DOI: https://doi.org/10.3390/catal9050429.

136. Heidinger, B., et al., Reactive grinding synthesis of LaBo3 (B: Mn, Fe) perovskite; properties for toluene total oxidation. Catalysts, 2019. 9(8): p. 633.
DOI: https://doi.org/10.3390/catal9080633.

How to cite this article: Batool SM, Kainat KE, Fazal S, Ahmad F. (2022). Comprehensive review on synthesis of abox material and its catalytic applications. Journal of Chemistry and Environment. 1(1).p.16-55.
https://doi.org/10.56946/jce.v1i01.49

Authors Bibliography

Dr. Fawad Ahmad received his Ph.D. degree in physical chemistry in 2018 from University of Science and Technology of China (USTC) under the supervision of Professor Jie Zeng Group at Hefei National Laboratory for Physical Sciences at Microscale USTC. He moved back to his homeland and join University of Wah, Wah-Cantt, Pakistan as assistant professor of chemistry in august 2019. His work is focused on synthesis of nanomaterials and its catalytic application for fuel cell and water decontamination.

Syeda Mehak Batool earned her MSc degree in chemistry from university of Wah in 2019. Currently she is pursuing MS in inorganic chemistry from the same university under the supervision of Dr. Fawad Ahmad, her research interest is synthesis of nano materials and its catalytic applications.

Khushboo E kainat earned her BS degree in chemistry from university of Wah in 2019. Currently she is pursuing MS in inorganic chemistry from the same university under the supervision of Dr. Fawad Ahmad, her research interest is synthesis of nanomaterial based novel catalyst.

Suqqyana Fazal earned her MSc degree in chemistry from university of Wah in 2021. Currently she is pursuing MS in inorganic chemistry from the same university under the supervision of Dr. Fawad Ahmad, her research interest is synthesis of nanomaterials and its application in catalysis, degradation and adsorption.